

# GEOTECHNICAL ENGINEERING RECONNAISSANCE OF THE 2010 HAITI EARTHQUAKE

Version 1: February 22, 2010



## CONTRIBUTING AUTHORS

**Ellen Rathje** (University of Texas, Austin, TX, USA)  
**Jeff Bachhuber** (Fugro/William Lettis & Associates, Walnut Creek, CA, USA)  
**Brady Cox** (University of Arkansas, Fayetteville, AR, USA)  
**Jim French** (AMEC/Geomatrix, Oakland, CA, USA)  
**Russell Green** (Virginia Tech, Blacksburg, VA, USA)  
**Scott Olson** (University of Illinois, Urbana-Champaign, IL, USA)  
**Glenn Rix** (Georgia Tech, Atlanta, GA)  
**Donald Wells** (AMEC/Geomatrix Oakland, CA, USA)  
**Oscar Suncar** (University of Texas Austin, TX, USA)

## OTHER CONTRIBUTORS

**Ed Harp** (US Geological Survey)  
**Paul Mann** (University of Texas)  
**Rich Koehler** (Alaska Division of Geology and Geophysical Surveys)

## **TABLE OF CONTENTS**

**1.0 INTRODUCTION**

**2.0 SEISMOLOGICAL ASPECTS**

**3.0 REGIONAL GEOLOGY**

**4.0 SURFACE FAULTING AND COASTAL UPLIFT**

**5.0 DAMAGE PATTERNS**

**6.0 PORT FACILITIES AND COASTAL INFRASTRUCTURE**

**7.0 LIQUEFACTION AND LATERAL SPREADING**

**8.0 ROAD FILL PERFORMANCE**

**9.0 LANDSLIDES**

## 1.0 INTRODUCTION

On January 12, 2010 a magnitude  $M_w$  7.0 earthquake struck the Port-au-Prince region of Haiti. The earthquake epicenter was located immediately west of the city of Port-au-Prince, and the damage induced by this event was extreme. It is estimated that over 200,000 people were killed during the earthquake, and several hundred thousand injured. A strike-slip  $M_w = 7$  event that affects ground near the margins of a bay represents a common earthquake scenario in the United States and throughout the world, and thus it was important to document the aspects of this event.

GEER mobilized a reconnaissance team, funded by the United States National Science Foundation, consisting of geotechnical engineers and engineering geologists from both the United States and the Dominican Republic. The team members included:

- **Prof. Ellen Rathje** (Team leader, University of Texas)
- **Mr. Jeff Bachhuber** (Fugro/William Lettis & Associates)
- **Prof. Brady Cox** (University of Arkansas)
- **Mr. Jim French** (AMEC/Geomatrix)
- **Prof. Russell Green** (Virginia Tech)
- **Mr. Juan Molina** (Constructora Inmobiliaria M&N)
- **Mr. Tabare Mundaray** (Proyectos Especiales)
- **Prof. Scott Olson** (University of Illinois)
- **Prof. Luis Pena** (Pontificia Universidad Catolica Madre y Maestra)
- **Prof. Glenn Rix** (Georgia Tech)
- **Mr. Oscar Suncar** (University of Texas)
- **Mr. Donald Wells** (AMEC/Geomatrix)

Glenn Rix was part of an advance team that partnered with EERI, the USGS, and the US Army Corps of Engineers to visit Haiti from 26 January to 2 February 2010. The remainder of the team travelled to Haiti, via the Dominican Republic, and was in country between 31 January and 5 February 2010. The GEER team also partnered in the field with Dr. Paul Mann of the University of Texas and Dr. Rich Koehler of the Alaska Division of Geology and Geophysical Surveys.

## ACKNOWLEDGMENTS

Primary support for the participants in this work was provided by grants from the U.S. National Science Foundation as part of the Geo-engineering Extreme Events Reconnaissance (GEER) Association activity through an NSF RAPID Grant and CMMI-00323914. Any opinions, findings, and conclusions or recommendations expressed in this material are those of the authors and do not necessarily reflect the views of the National Science Foundation.

Additional support for our efforts was provided by security personnel from Haiti (Francois Aurel, Alex, and Jack) and by Mr. Rick Sellers, the security manager for AMEC/Geomatrix. GPS street maps for Haiti were donated to the team by GPSTravelMaps.com. These maps were extremely useful during the reconnaissance. This support is gratefully acknowledged.

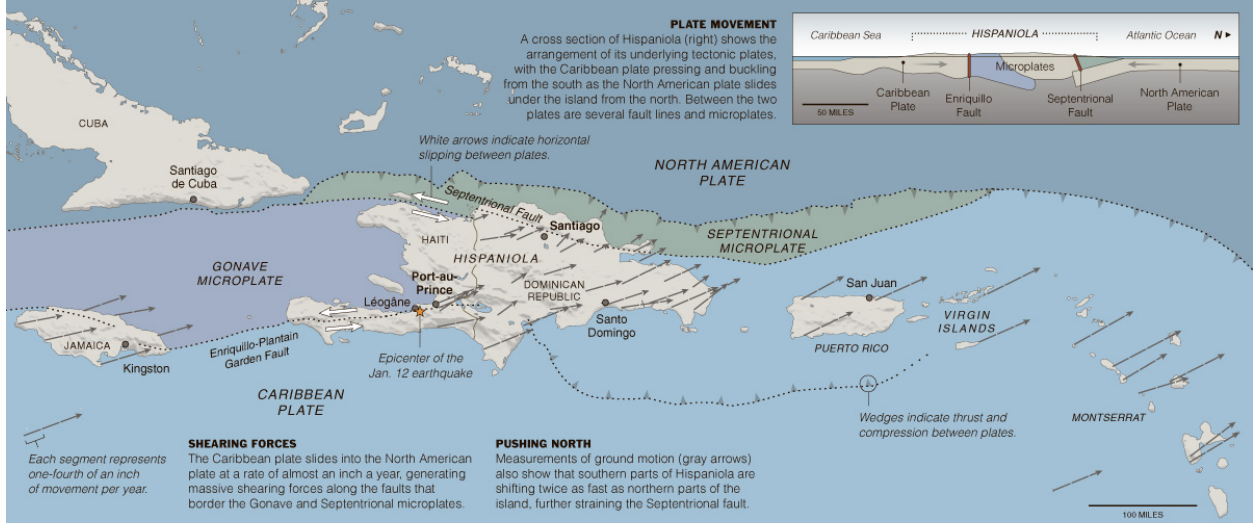
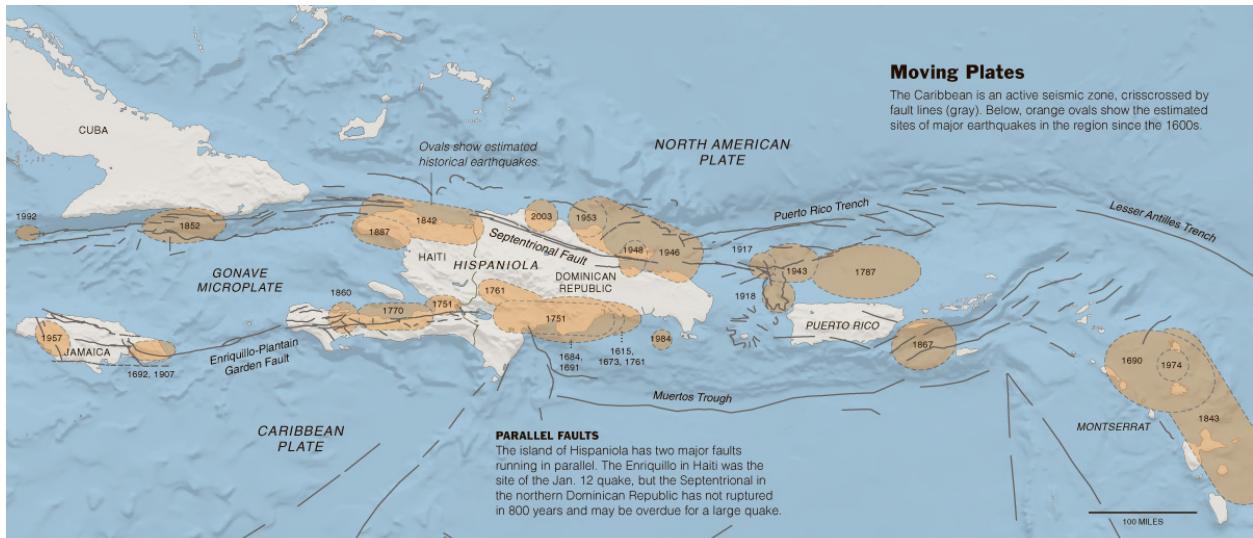
GEER Recorder Katherine Jones assisted with the preparation and posting of the report.

## 2.0 SEISMOLOGICAL ASPECTS

Haiti occupies the western third of the island of Hispanola, along the northern boundary of the Caribbean plate (Figure 2.1). The island occurs on a separate microplate bounded on the north by the Great Puerto Rican/North Hispanola subduction zone and transtensional strike-slip faults (Oriente-Septentrional fault) that define the boundary between the North American and Caribbean plates, and the Muertos trench subduction zone and strike-slip Enriquillo-Plaintain Garden fault zone (EPGFZ) that define the plate interface between the microplate and Caribbean plate (Figure 2.1).

The  $M_w = 7.0$  Haiti earthquake occurred at 4:53 PM local time on January 12, 2010. The USGS reports that the earthquake epicenter was located at 18.457N, 72.533W, approximately 25 km west of the city of Port-au-Prince. The earthquake was initially presumed to have occurred on the Enriquillo-Plantain Garden Fault Zone (EPGFZ), a left-lateral, strike-slip fault that slips approximately 7 mm/yr (Figure 2.1). Although the EPGFZ is a strike-slip fault, the focal mechanism for this earthquake was identified as left-lateral/oblique. Additionally, as noted in Section 4.0 Surface Faulting and Coastal Uplift, the EPGFZ did not rupture at the surface and significant uplift occurred north of the EPGFZ, such that there is significant uncertainty regarding the causative fault for the earthquake. Large earthquakes have not occurred recently on the EPGFZ, but historical records indicate that Port-au-Prince was destroyed by earthquakes in both 1751 and 1770. These events are believed to have occurred on the EPGFZ (Figure 2.1).

Fault rupture inversions have been developed for this event by various researchers, including the USGS. One fault rupture inversion, generated by Anthony Sladen of Caltech ([http://tectonics.caltech.edu/slip\\_history/2010\\_haiti/](http://tectonics.caltech.edu/slip_history/2010_haiti/)) using broadband teleseismic data, is shown in Figure 2.2. This inversion indicates that the fault rupture was concentrated along a 20 km segment west of the epicenter, with a maximum slip of about 4 m. Interestingly, a significant vertical component of slip is shown starting at about 10 km west of the hypocenter. This vertical component of slip is consistent with the identified focal mechanism and was corroborated by observations of coastal uplift in this area (see Section 4.0 Fault Rupture and Coastal Uplift). The derived Source Time Function (STF) for this event (Figure 2.2) indicates that the majority of the seismic moment was released in a relatively short time, approximately 6 seconds. A similar rupture pattern was reported by other slip inversions.



Sources: Paul Mann, University of Texas at Austin; Eric Calais, Purdue University; Geological Society of America; American Geophysical Union; U.S. Geological Survey; Gebco; Collins Bartholomew  
JONATHAN CORUM/THE NEW YORK TIMES

**Figure 2.1** Historical earthquakes and fault zones in the region around the island of Hispaniola (New York Times, January 26, 2010)

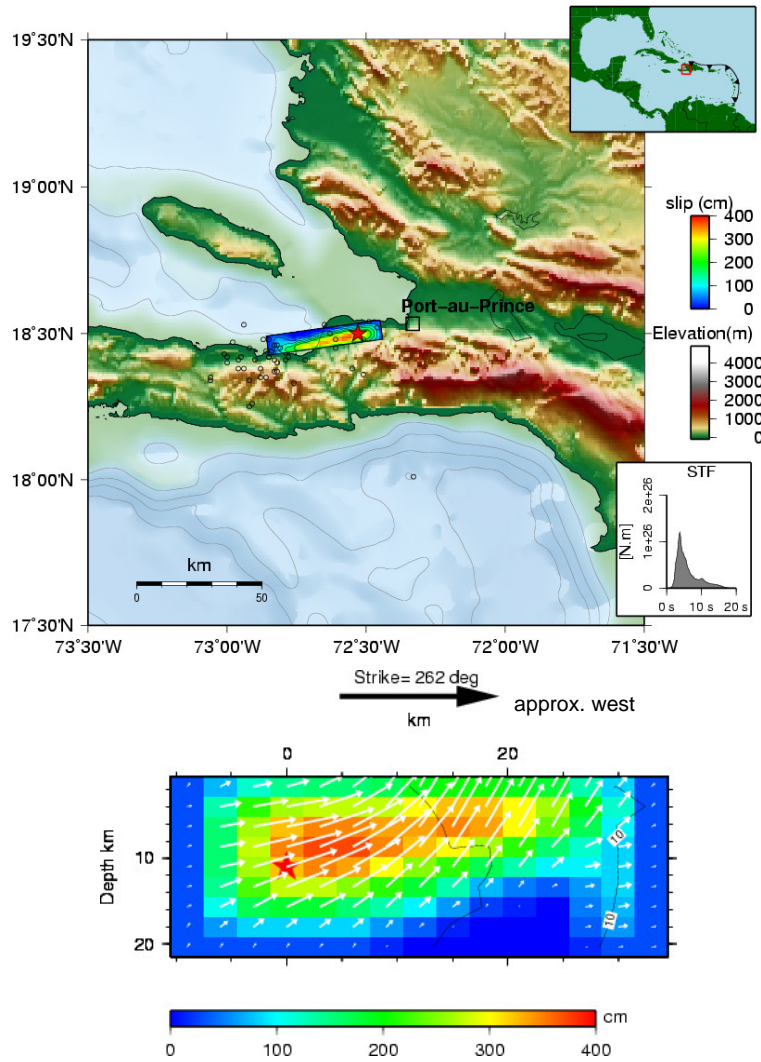


**Figure 2.2** Slip distribution for the 2010 Haiti earthquake derived from teleseismic data ([http://tectonics.caltech.edu/slip\\_history/2010\\_haiti/](http://tectonics.caltech.edu/slip_history/2010_haiti/))

The preliminary locations for aftershocks located by the regional seismic data are shown in Figure 2.3, along with the slip inversion derived by Caltech. The aftershocks extend over a distance of about 50 to 60 km, predominantly westward from the epicenter, and generally scattered along the trace of the Enriquillo Plantain Garden fault. There is a distinct clustering of aftershocks about 30 km west of the epicenter (near Petit Goave), which corresponds with the end of the fault rupture inferred from the slip inversion as well as an extensional stepover in the fault. This extensional stepover (identified as the Miogoane Lakes Basin extensional stepover in Figure 3.2 of Section 3.0 Regional Geology) is a natural segmentation point for the fault, and together with the other data shown in Figure 2.3, appears to have arrested the westward progressing fault rupture. Therefore, it appears that the major portion of the mainshock rupture process was only about 30 km long. This is somewhat shorter than would be expected for M 7 earthquake as estimated from empirical relationships (e.g., Hanks and Bakun 2008, Wells and Coppersmith 1994) that predict a rupture length of about 50 km for a M 7 earthquake. However, comparisons of rupture lengths estimated from the earthquake rupture process versus the distribution of aftershocks are not generally reliable or definitive.

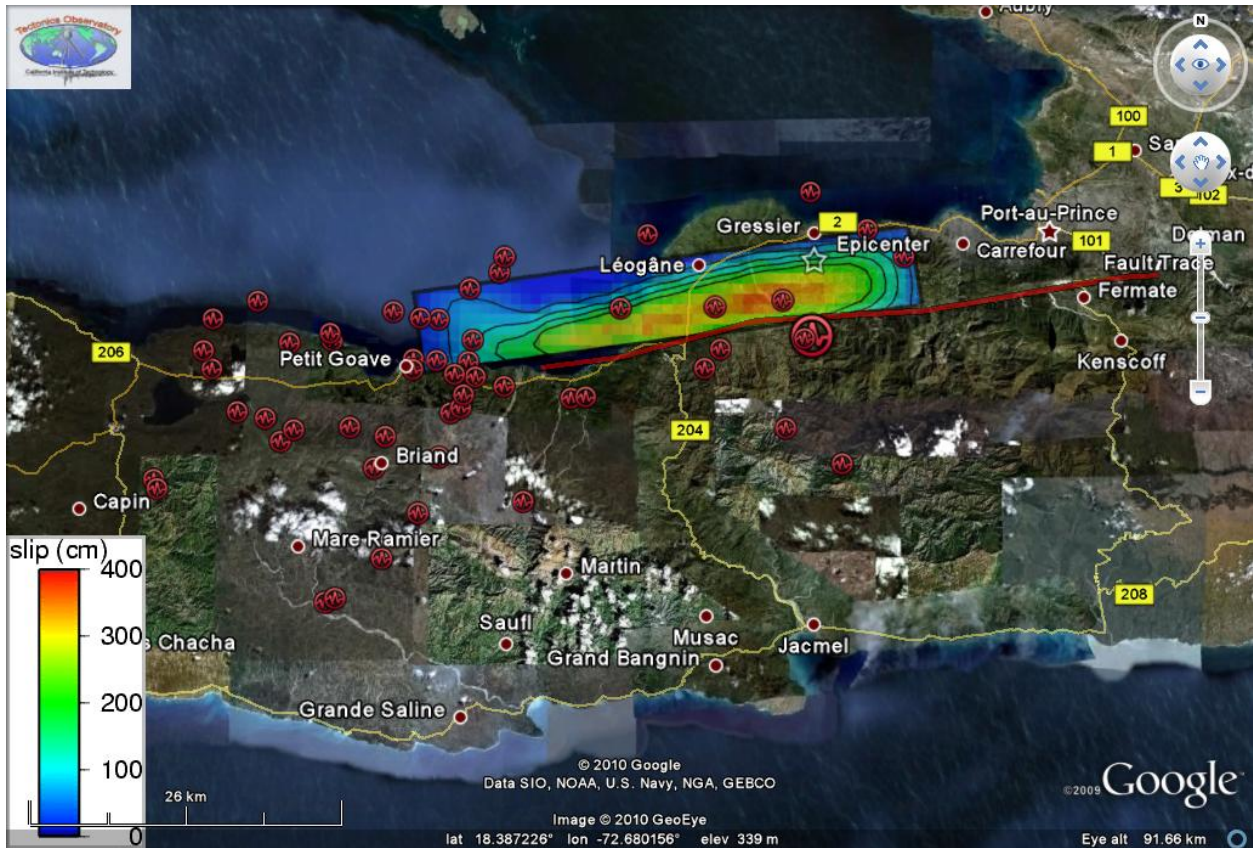


**Figure 2.3** Aftershock distribution for the 2010 Haiti earthquake through 21 January 2010 (from USGS), along with slip inversion by Caltech

The USGS ShakeMap of Instrumental Intensity for the near-fault region is shown in Figure 2.4, and indicates violent to extreme shaking in the area around Port-au-Prince. Because there were no strong motion stations within 100 km of the fault rupture, the ShakeMap Instrumental Intensity information was derived solely from the magnitude of the earthquake, the location of the earthquake, empirical ground motion prediction models, and observed macroseismic intensities reported on the USGS Did You Feel It? website. Nonetheless, the ShakeMap zones of IX and X (shown in red) generally correspond with the hardest hit areas of the region. The USGS ShakeMaps for peak ground acceleration (PGA) and peak ground velocity (PGV) are shown in Figure 2.5, and were derived from the estimated Instrumental Intensities (i.e., Figure 2.3) and far field ground motions recorded in the Dominican Republic. These ShakeMaps estimate the largest PGA to be about 0.3 g and the largest PGV to be about 80 cm/s. These estimates should be considered very approximate because of the lack of strong motion recordings.

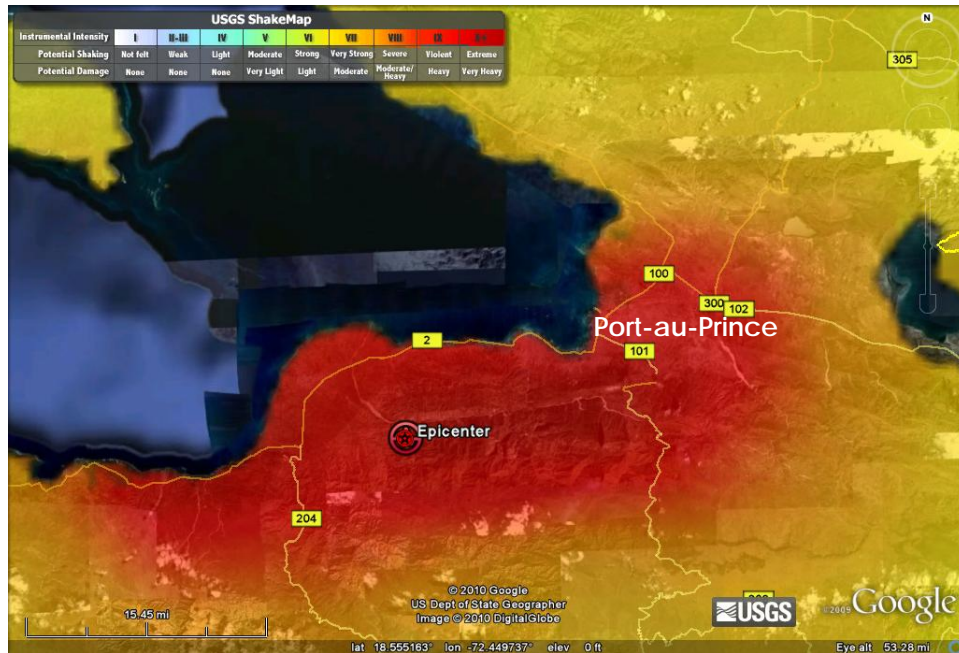


**Figure 2.4** USGS ShakeMap of Instrumental Intensity for the near-fault region.

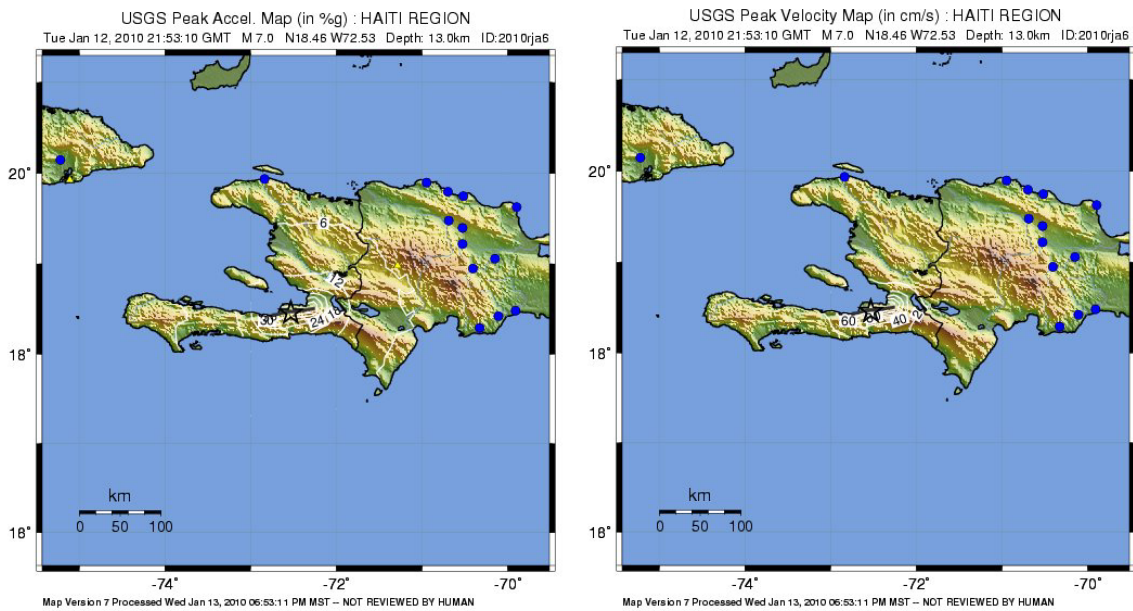


**Figure 2.5** USGS ShakeMaps of PGA and PGV for the island of Hispaniola.

## References

- Hanks, T.C. and Bakun, W.H., 2008, M-logA Observations for Recent Large Earthquakes: Bull. Seism. Soc. Am. 98, 490 - 494.
- Wells, D. L., and Coppersmith, K.J., 1994, New empirical relationships among magnitude, rupture length, rupture width, rupture area, and surface displacement: Bull. Seism. Soc. Am. 84, 974-1002.

### 3.0 REGIONAL GEOLOGY

The epicentral zone of the January 12 Haiti earthquake extends roughly from the Port-au-Prince alluvial valley in the south central part of the country, eastward to the vicinity of Petite Goave along the north coast of the Haitian southern peninsula. Section 2.0 of this report, Seismological Aspects, describes the seismology and earthquake mechanics, and presents a figure showing the epicentral zone of strong shaking (Figure 2.3).

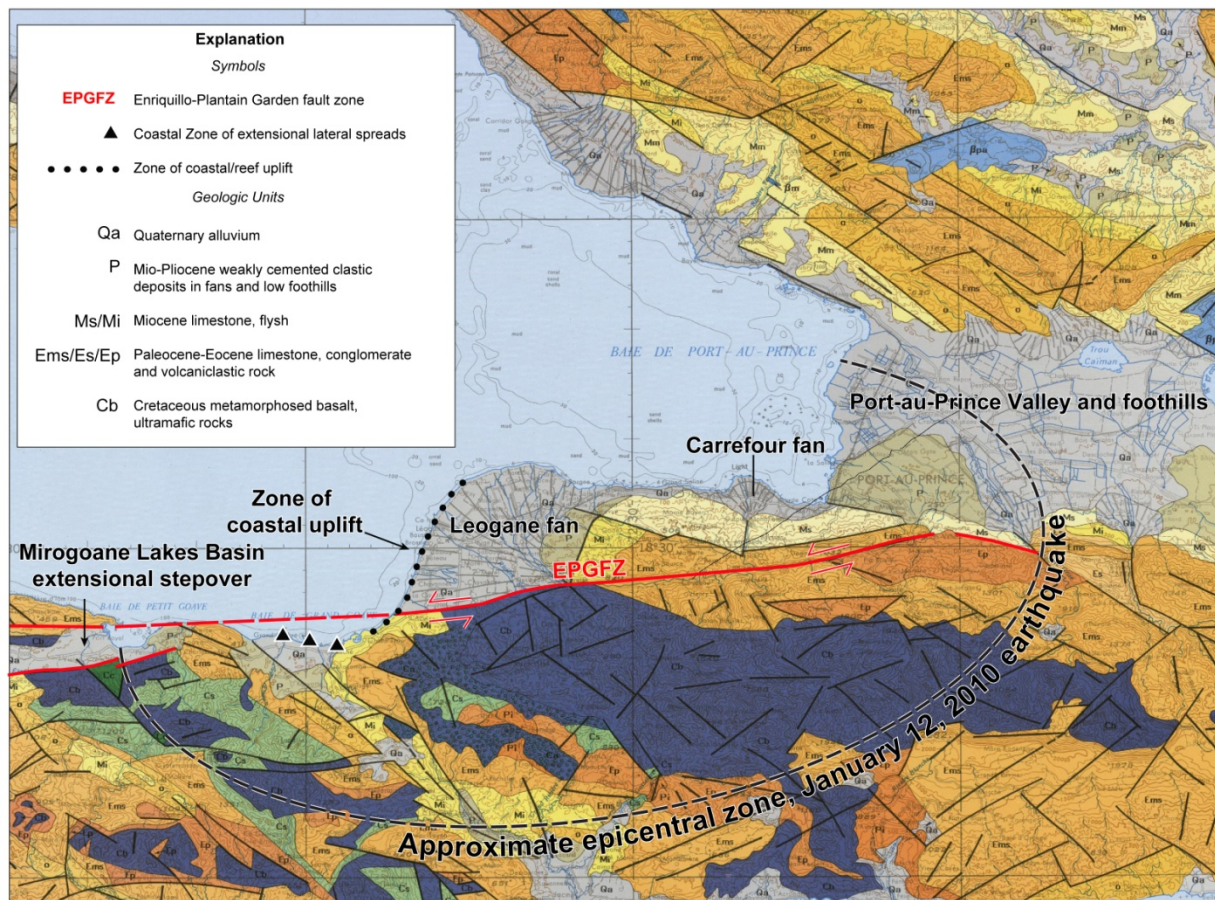


**Figure 3.1.** View west of Enriquillo Plantain Garden fault zone. Fault extends west-southwest from Pétion-ville along the prominent linear valley of the Frorse and Momance rivers at center of picture. Epicenter of 12 January M 7.0 earthquake shown by red star. The rupture extended west from the epicenter, away from Port-au-Prince.

The earthquake occurred on the Enriquillo-Plantain Garden fault zone (EPGFZ), a major tectonic element with a long history of deformation and slip. The fault traces roughly west-east along the north portion of the southern Haiti peninsula (Figure 3.1), and has exerted a substantial topographic/geomorphic influence since the Tertiary. Quaternary displacement along the fault has formed a classic strike slip fault geomorphology including linear valleys and bounding uplifted mountains, shutter ridges, sag ponds, and elliptical basins at extensional stopovers and bends along the fault trace. Some stream reaches, such as within the deep valley of the Frorse and Momance rivers that follows the EPGFZ trace, are apparently the result of both stream capture by recent displacements along the fault and preferred incision along sheared and locally weaker rocks along the fault zone (Figure 3.1). Additional discussion of the relationship between topographic features and the EPGFZ, and Quaternary geomorphic expression, are discussed in Section 4.0 of this report. Surprisingly, no evidence of surface fault rupture has been found by the GEER team or other field teams. These investigations have included visits to

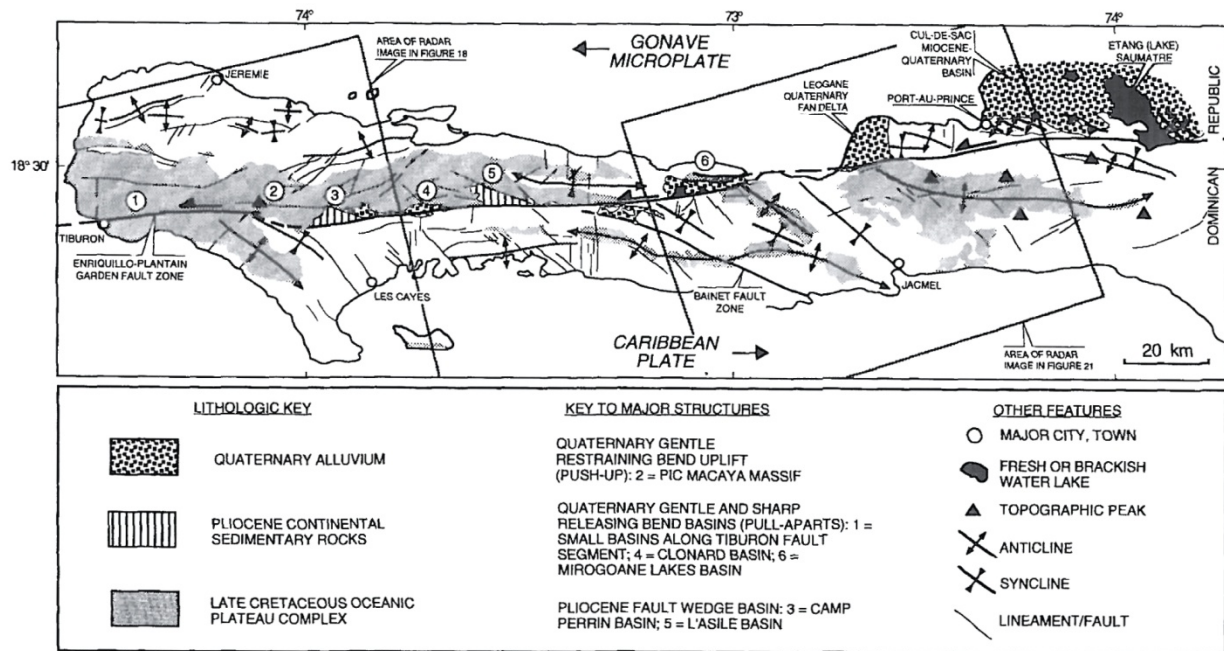
multiple reaches of the fault in the epicentral zone that have clear Quaternary-active geomorphic expression, and roadways/tracks that cross perpendicular or obliquely across the entire well-expressed fault zone.

The earthquake-affected region is a physiographically diverse area that has undergone a complex geologic history of intrusion, tectonism, erosion, and sedimentation. The topography within the study area is relatively rugged, with steep mountain ranges and hillfronts, deeply incised streams and narrow intermountain stream valleys, and broad coastal delta fans and valleys. Figure 3.2 is a geologic map of the earthquake epicentral area, based on original mapping by C.E.R.C.G. IMAGEO (Lambert, Gaudin, and Cohen, 1987). The map shows the central mountainous core of the southern peninsula to be locally underlain by metamorphosed Cretaceous basalt/mafic volcanic basement, and Cretaceous-Eocene limestone, conglomerate, and clastic sedimentary rocks. An east-west trending band of Miocene and Mio-Pliocene sedimentary rock (including flysch, siltstone, shale, sandstone) occurs along the coast and southern margin of the Port-au-Prince alluvial valley. Contacts between the Miocene and Mio-Pliocene units are commonly faulted, and small folds and possible thrust faults have deformed the Mio-Pliocene bedrock in response to a regional northeast-southwest compression, oblique to the trend of the strike-slip motion along the EPGFZ (Figure 3.3).



Modified from country-wide map by C.E.R.C.G. IMAGEO (Lambert, Gaudin, and Cohen, 1987).

**Figure 3.2** Geologic map of January 12, 2010 Haiti earthquake epicentral area.



Note:  
Tectonic map of the southern peninsula of Haiti (modified from Mann, 1983, and Vila et al., 1985). Numbers are keyed to major strike-slip-related structures listed on the map key. Boxes indicate locations of radar images interpreted in Figs. 18 and 21.

Figure 3.3. Regional structural geologic map. (Mann et al 1995)

Quaternary deposits in the earthquake epicentral zone include Holocene to late Pleistocene fluvial alluvium (channel, terrace, floodplain overbank deposits) deposited in the Port-au-Prince valley and interior incised river valleys, alluvial fan and colluvial wedge deposits along the margins of larger valleys, coastal delta fan complexes where larger streams (e.g., Momance and Frorse Rivers) discharge into the sea along the coast, localized organic sediments within marshes and swamps, and beach sands along protected portions of the coast. The central area of Port-au-Prince which was devastated by the earthquake spans from the relatively level floor of a large alluvial valley, southward onto low hills underlain by Mio-Pliocene deposits. Portions of the city are presumably underlain by thick sequences of Holocene to Pleistocene alluvium in a broad downwarped basin, but zones of high damage extend onto the Mio-Pliocene bedrock. The cities of Leogane (Figure 3.1, which experienced a high percentage of structurally collapsed buildings and extensive shaking damage) and Carrefour (Figure 3.1) are located on large delta fans, and underlain by a thick sequence of Holocene to Pleistocene alluvium.

The distribution of most dense or severe building damage from the earthquake appears to be at least in part correlative with geologic conditions (see Section 5.0 Damage Patterns). Amplified shaking likely occurred as a result of thick alluvial soils in the north-central and coastal region of Port-au-Prince, Carrefour, and Leogane. However, large zones of extensive and dense damage occurred in the southern portion of Port-au-Prince that extends onto the hills underlain by Mio-Pliocene, weakly-cemented deposits. Although these deposits are quite stiff and not generally perceived as representing a significant amplification hazard (e.g., Building code Vs30-based soil classification) other mechanisms of amplification may have been at work, such as topographic amplification, distributed slip/deformation along folds and blind faults, seismic wave focusing along geologic structures (folds and blind thrust faults), or basin margin

effects. These effects may have contributed to higher levels of shaking or adverse frequency content in these materials. The correlation between geologic conditions and damage is discussed in Section 5.0 of this report. Filled ground in port areas of Port-au-Prince and Carrefour experienced classic liquefaction, lateral spread, and settlement damage. Port liquefaction and effects are discussed in Section 6.0 Port Facilities and Coastal Infrastructure.

Older Quaternary (Pleistocene) deposits include elevated sand and gravel fluvial terraces along major streams, older (inactive) portions of delta fans, and elevated coastal marine terraces. Some of the larger, older (late Pleistocene) alluvial fan complexes occur at the mouths of drainages along the south and north margins of the Port-au-Prince alluvial valley, and North Coast between L-accueil and Gran Goave. Urban expansion south of Port-au-Prince and Carrefour extends onto the Mio-Pliocene bedrock hills and older alluvial fans.

The sediment carried by the active river systems is dominated by sand and gravel within braided channel systems in intermountain valleys and the mouths of canyons, and a distally-fining sequence of fine sand, silt, and clay at the distal ends of delta fans, coastal lowlands/marshes, and interior areas of larger alluvial valleys. Delta fans and alluvial valleys show evidence of relatively rapid sedimentation and considerable migration of active drainages through the Quaternary. As a result, distinct active and older sediment “lobes” or terraces can be differentiated based on elevation, degree of erosional modification, and soil development. Most of the large lateral spreads that occurred during the earthquake developed within artificial fill along the coast (e.g., Port-au-Prince and Carrefour ports), or at the distal noses of delta fans that are prograding into the sea between Leogane and Gran Goave. These failures are discussed in Sections 6.0 and 7.0 of this report.

Many of the road failures observed along the coast west of Carrefour occur where the road crosses marshy ground and the distal ends of small alluvial valleys. Settlement and localized creep/slumping of sediments underlying the road bed appears to be responsible for many of the road failures, rather than lateral spread failure, as cracking typically was confined to the road beds and fill, and does not extend through natural soils shoreward of the roadways. Localized liquefaction of loose, saturated sediments in these areas may have contributed to the road failures, but was not the major factor, as discussed in Section 8.0 of this report.

Numerous landslides and rockfalls occurred within the Mio-Pliocene and older limestone bedrock in steep slopes and roadcuts within the epicentral zone. In some cases these failures appear to have been restricted to colluvial soil and fractured/dilated rock within a weathered zone that extends about 1 to 3 m deep into the slopes. However, some deeper-seated slumps and debris avalanche/slide failures occurred in less-weathered, deeper bedrock in steep mountainous slopes. These failures appear in part to be influenced or controlled by bedrock joints or weak zones. Developments on steep slopes in places appear to have been impacted by slope raveling or foundation sliding/slumping, but appear to have been primarily damaged by possible topographically-induced amplified shaking or structural/design dictated by development on steep slopes (e.g., tall, slender columns on downhill sides of buildings constructed on steep slopes). These issues are discussed further in Section 9.0 of this report.

## References

P. Mann, F.W. Taylor, R.L. Edwards, T.-L. Ku (1995) “Actively evolving microplate formation by oblique collision and sideways motion along strike-slip faults: An example from the northeastern Caribbean plate margin,” *Tectonophysics*, 246, p. 1-69.

## 4.0 SURFACE FAULTING AND COASTAL UPLIFT

### 4.1 Introduction

Surface fault rupture, which is a manifestation of the fault displacement at the ground surface, often occurs as a result of moderate- to large-magnitude earthquakes ( $M \sim 6$  or larger) occurring on active faults having mapped traces or zones at the ground surface. The likelihood of and amount of displacement during surface rupture is a function of earthquake magnitude, focal depth, fault geometry, earthquake rupture process, nature of near surface soils and bedrock, and occurrence of fault creep. The amount of surface fault displacement can be as much as 1 to 5 meters or more, depending on the earthquake magnitude and other factors. The displacements associated with surface fault rupture can have devastating effects on structures and lifelines situated astride the zone of rupture. While in most cases the easiest mitigation for surface rupture is avoidance, in some cases (i.e., lifelines, such as buried water, natural gas, or petroleum pipelines, or existing structures) it may be necessary to design mitigation to accommodate fault displacement while meeting specified performance objectives. Therefore, it is important to document the occurrence or non-occurrence of surface rupture, and if present, to document the location, fault geometry and displacement, nature of soil or bedrock at the surface, and effects on overlying structures.

Surface fault rupture is typically expected to occur along geomorphically well-expressed faults, such as the Enriquillo-Pantain Garden fault zone (EPGFZ), and during large magnitude, shallow earthquakes, such as the January 12, 2010 Haiti earthquake. Well-exposed reaches of the fault, roadways and pavements crossing the fault trace, and young geologic layers or geomorphic surfaces across the fault were targeted to examine for surface fault rupture or deformation.

### 4.2 Fault Rupture Investigations

The EPGFZ is well expressed across southern Haiti, passing through Pétion-ville and south of Port-au-Prince (Figure 3.1). As described in Section 3.0, the fault is characterized by linear valleys and bounding uplifted mountains, shutter ridges, sag ponds, and elliptical basins at extensional stopovers and bends along the fault trace (Figures 4.1, 4.2, and 4.3). The presence of these and other well defined geomorphic features that define the fault trace at the surface indicate that the fault has ruptured repeatedly at the ground surface in large magnitude earthquakes in the past. Therefore, given that most shallow crustal earthquake of  $M 7.0$  have ruptured to the ground surface (Lettis et al. 1997), and given the location of the epicenter near the EPGFZ and the dominantly strike-slip nature of the earthquake focal mechanism, it was anticipated by most geologists that surface rupture would have occurred on the EPGFZ.

The GEER team conducted reconnaissance at several sites along the EPGFZ to assess whether the fault ruptured at the ground surface. The reconnaissance was coordinated with other researchers (Dr. Paul Mann of the University of Texas Austin, Dr. Rich Koehler of the Alaska Division of Geology and Geophysical Surveys, and Dr. Roger Bilham of the University of Colorado) who also were searching for evidence of fault rupture. Dr. Mann and Dr. Koehler conducted reconnaissance along the EPGFZ in the area east of Dufort and Fayette, including visiting several sites along the prominent linear valley east of Fayette (Figures 4.1 and 4.2). These sites were near and east of the epicenter of the earthquake, and the reconnaissance conducted by the other scientists documented that surface rupture had not occurred on the fault in the area of the epicenter and further east along the prominent linear fault valley. The GEER team met with Dr. Mann and Dr. Koehler, and two representatives from the Haitian Bureau of Mines and Energy on February 1 for the purpose of conducting reconnaissance along areas of the

EPGFZ west of the epicenter. The reconnaissance conducted by the GEER team focused on the central and western parts of the fault rupture zone identified from the aftershock locations, which encompassed an area extending about 50 km west from the epicenter (Figure 2.3). The observations made during reconnaissance and preliminary mapping of fault traces are described in this section.



**Figure 4.1.** View east towards Fayette and Leogane along parallel east-northeast trending traces of Enriquillo Plantain Garden fault. Fault trace marked by push-pins labeled “EPG flt”. Fault trace at right (left offset of river along prominent north-facing scarps) apparently steps north to linear valley of Momance River at top left of picture.

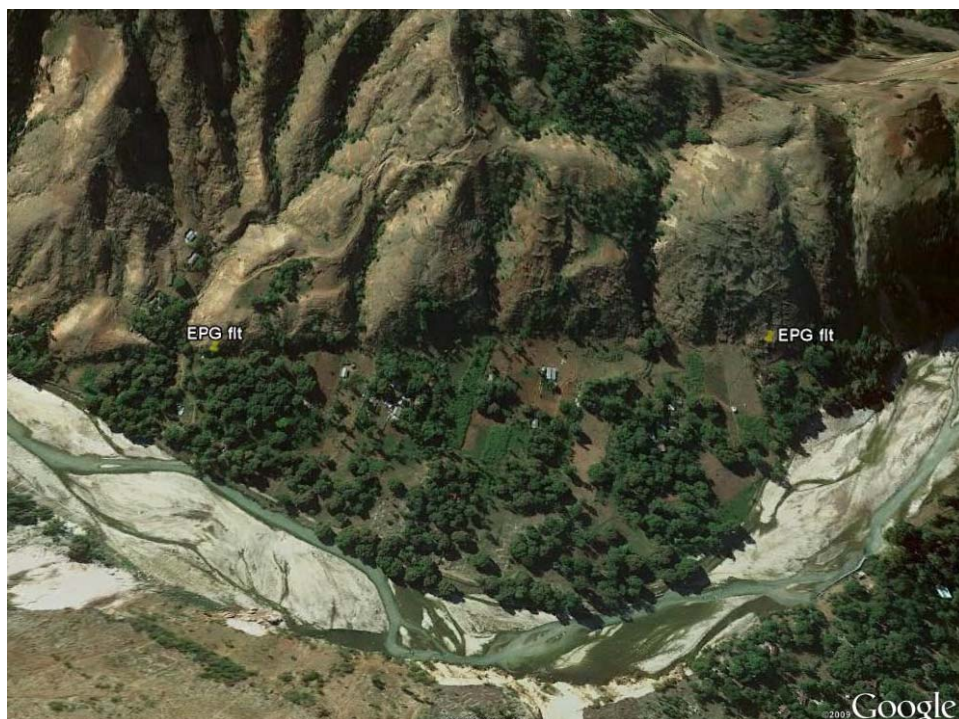


**Figure 4.2.** View south of prominent fault scarp crossing fluvial terrace on Momance River east of Fayette. Fault trace marked by push-pins labeled “EPG flt”.

Dr. Mann and Dr. Koehler identified several locations near Dufort where the location of the EPG fault was well constrained and accessible, and the combined team visited these sites on February 1. These sites are located along Road 204 (Jacamel Road) and west of Road 204 (Figure 4.3). Road 204 passes south from the intersection with Road 2 across the plain and up the slope of the east-west trending mountain range. The EPG fault lies along the base of the range, at a prominent break-in-slope from the plains to the lower part of the range. The team confirmed that Road 204 is not displaced where it crosses the fault and range front. A distinct linear valley and shutter ridge occur at the base of the hills about 0.75 km west of Road 204, providing a well-constrained location of the active trace of the EPG fault. The team inspected the fault over a distance of several hundred meters across the small valley, along several transects extending across the shutter ridge and through the valley bottom to bedrock areas exposed on the hillslope above the valley. The fault is constrained to lie at the prominent break-in-slope at the base of the hill or within a few tens of meters east in the valley bottom (Figure 4.4). South of this valley, the EPGFZ is marked by the prominent break-in-slope and a series of side-hill benches (Figure 4.5). The team observed minor cracking in the valley floor at one location, and a linear north-facing scarp at the base of the hillslope. It was concluded that the minor cracking in the valley floor likely represented effects of shrink-swelling in the soil and that the north-facing scarp was the result of hoeing/tilling for agricultural purposes (Figure 4.6). Therefore, the team concluded that the fault did not rupture at the ground surface through the small valley.

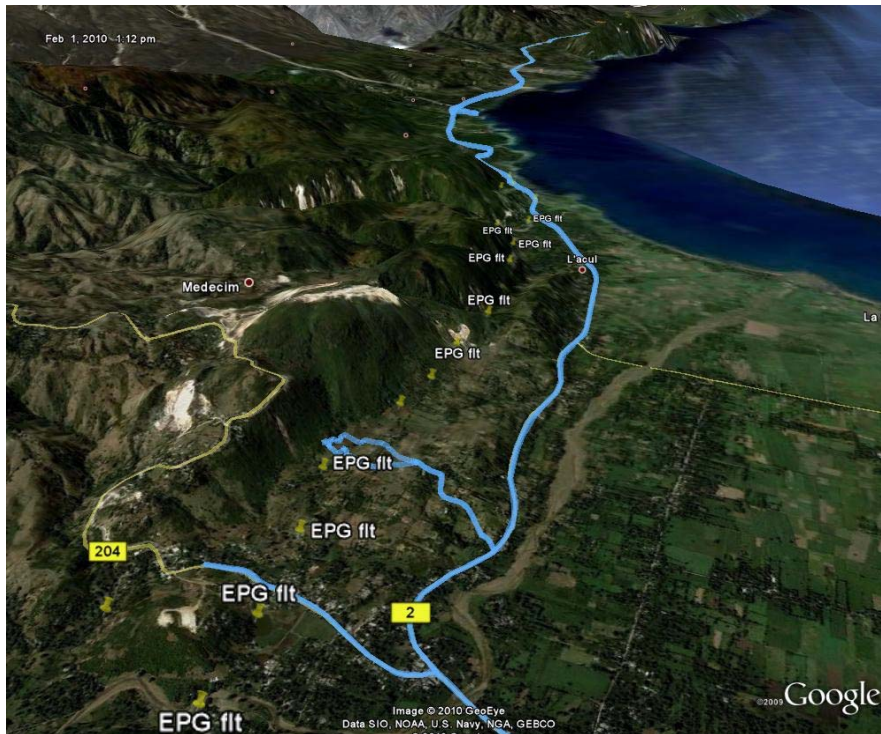


**Figure 4.3.** View southwest along EPG fault west of Dufort. Reconnaissance track marked in blue shows location of fault traverses on and west of Road 204. Fault trace marked by push-pins labeled “EPG flt”.



**Figure 4.4.** View west along trace of EPG fault at linear valley southwest of Dufort (west of Road 204). Fault trace likely between base of slope (between red arrows) and center of linear valley. No fractures or other evidence for fault rupture observed at this site (N18.444306, W72.643722,).



**Figure 4.5.** View east along trace of EPG fault from hill above linear valley west of Road 204 (along red arrow) (N18.445819, W72.6431718).



**Figure 4.6.** View west along agricultural scarp in linear fault valley west of Road 204 (N18.444527, W72.643777).



**Figure 4.7.** View south of shutter ridge blocking drainage (center) and offset stream channel (center right) along fault south of L’acul. Fault trace marked by push-pins labeled “EPG flt”.

The GEER team traversed Road 2 west of Road 204, where Road 2 is parallel to and crosses over the EPGFZ near L’acul, on several occasions between February 1 and 4 during additional reconnaissance investigations (Figure 4.7). No evidence of lateral road displacements or equivocal shear cracks was found on the roads across the fault crossing areas. However, a number of cracks and areas of settlement were observed along the road. These features were evaluated and we concluded to be the result of settlement of the road fill/embankment settlement over soft subgrade soils (see Section 8.0 Road Fill Performance), and possibly in some cases due to localized liquefaction. None of these features were found to represent surface fault rupture.

The EPGFZ extends along the base of the range for about 2.5 km west-southwest from L’acul, and passes offshore into Grand Goâve Bay. The fault apparently bends or steps northward in the offshore region, and then extends west-northwest along the coast to Petit Goâve Bay at Port Royal, approximately 20 km further west. The bend or step northward would be on the order of 1.5 to 2 km wide, or possibly wider, based on a westward projection of the EPGFZ fault from L’acul, and an eastward projection of the EPG fault from Port Royal. At the coast at Port Royal, the EPG passes along the base of the prominent steep linear south-facing range front, and extends west-northwest along the base and lower portion of the hillslope. Numerous offset drainages and side hill benches are visible on aerial imagery, with two parallel fault traces extending along the base and lower portion of the range front.

With the assistance of a local resident to guide the team along un-improved cart and horse paths off the paved road, the GEER team conducted traverses across the fault on February 4 at two locations in the area north and west from Port Royal (Figure 4.8). At the two sites, which were located along about a  $\frac{3}{4}$  km length of the range front, two parallel fault traces are marked by prominent side hill benches, offset drainages, and a sharp steeply dipping contact between colluvium and limestone bedrock (Figures 4.9 to 4.11). The team traversed footpaths that extended north upslope across the fault at both sites. No fracturing or evidence for fault rupture

was observed at the bedrock-colluvial contact (a northern fault trace) or along the base of the side-hill benches and alignment with diverted drainages (a southern fault trace). When asked whether and where they had observed any ground cracking, several local residents described ground failures due to landsliding on slopes on the opposite side of the valley, and one location of ground cracking on the coast east of Port Royal. We were not able to travel to the coast to evaluate the ground cracks because of impending darkness, but based on the description of the cracks as being near the water, and due to the prevalence of lateral spreading along the coast, it is likely that these fractures were due to ground failure rather than fault rupture. Thus, based on our observations and the information from the local residents, the team concludes that the EPGFZ did not rupture at the surface where it extends onshore from Petit Goâve Bay.

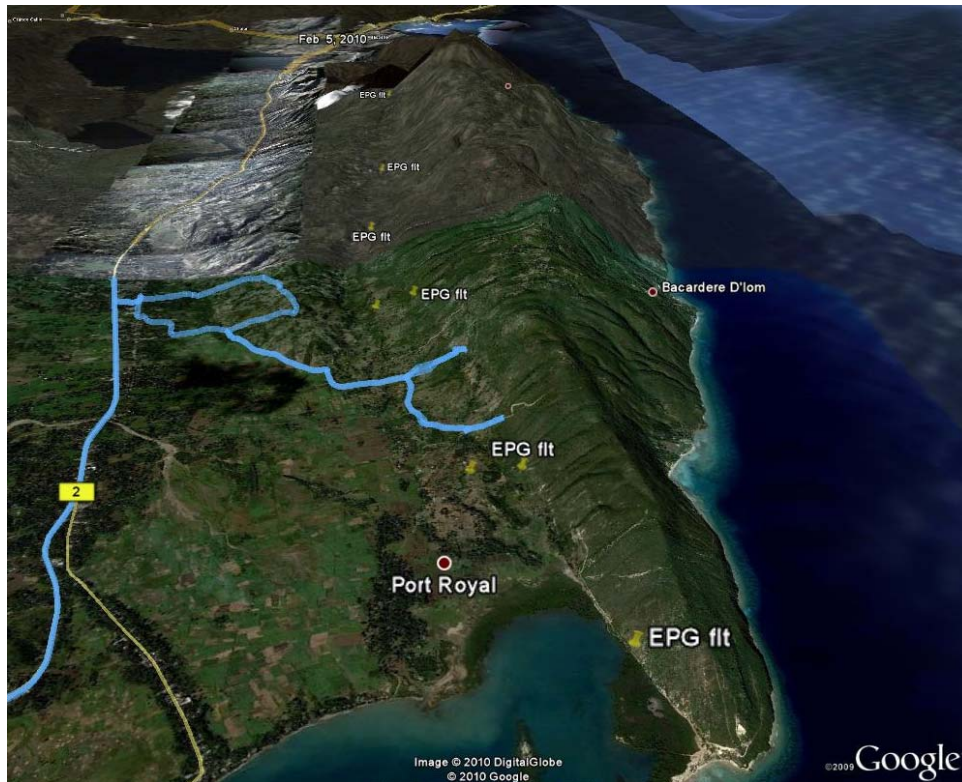


**Figure 4.8.** View west of prominent parallel west-southwest trending fault traces along south-facing slope of hills west of Petit Goâve Bay and Port Royal. Reconnaissance track marked in blue shows location of fault traverses west of Port Royal. Fault trace marked by push-pins labeled “EPG flt”.



**Figure 4.9.** View east-northeast along fault west of Port Royal. Side-hill bench bounded by two fault traces at left and center of photo (above red arrows). No fractures or other evidence for fault rupture observed at this site (N18.440027, W72.923304).



**Figure 4.10.** View north across fault (at upper break in slope) west of Port Royal. Side-hill bench and blocked drainages at center of photograph (between red arrows) (N18.439666, W72.916444).



**Figure 4.11.** View north across fault at west of Port Royal. Fault passes perpendicular to track in middle of photograph at colluvium-bedrock contact (at red arrows upslope from team members). No fractures or other evidence for fault rupture observed at this site (N18.44150, W72.916389).

### 4.3 Coastal Uplift

Coastal uplift, while not typically a life or structural damage hazard, has implications on performance of infrastructure dependent on maintenance of static grade (e.g. gravity storm drains, port facilities), and also influences general drainage and flooding patterns. Additionally, uplift represents evidence of broad, vertical crustal movements associated with fault rupture, and thus observations of coastal uplift help confirm the focal mechanism and slip distributions inferred from teleseismic data.

Interpretation of aerial imagery and reports from Haitians in the coastal area of Léogâne indicated that several areas along the coast were uplifted as a result of the 12 January earthquake. The GEER team traveled to the Ca Ira area west of Léogâne on 1 February to observe one area where coastal uplift had been observed. At this site, the team observed an area of exposed coral and subtidal Turtle grass extending for more than 100 m seaward from the shoreline (Figure 4.12). Key observations from this area are as follows.

Turtle grass is a subtidal plant, and apparently does not grow in areas exposed at low tide. As observed during our reconnaissance, an extensive area of this grass was exposed above the water level (which was at or close to low tide during our reconnaissance). Much of the exposed grass was brown and appeared to be dying as a result of exposure to air/direct sunlight (Figure 4.13). The length of the grasses was about 10 cm, possibly indicating the minimum submergence depth at low tide prior to the 12 January earthquake.

The coral reef exposed at low tide consisted of largely dead coral heads (Figure 4.14), with small areas of new living coral at the top of the heads (Figure 4.15). The outer coral head is dead, which appears to indicate that uplift occurred previously at this site, followed by submergence and growth of new coral. The minimum subtidal depth at which coral grows is dependent on the specific coral species and other factors, but may be on the order of several tens of centimeters.

Local villagers indicated that the grasses and mud flats were not exposed at low tides prior to the 12 January earthquake, and that the high tides no longer extended to the sea wall as indicated by the water marks on these walls (Figure 4.16). The current tide chart for Port-au-Prince indicates the tidal range typically is about 0.4 to 0.6 m.

The estimated uplift resulting from 12 January earthquake is on the order of 50 centimeters based on elevational differences between pre-event high tide marks on a seawall (interpretation by Rich Briggs), tidal records for the date and time of the field visit, elevation of current high tide debris strandline, presence of living coral exposed in the coral head above the water (Figure 4.17), the height (length) of the exposed grasses, and reports on water level/tidal changes by local villagers.



**Figure 4.12** Aerial view of coastal uplift in Ca Ira, near Legwane.  
(See GEER Haiti Report.kmz for location)



**Figure 4.13.** Reconnaissance team inspecting exposed grass and coral at Ca Ira, Léogâne. An extensive area of mud flats, grasses, and coral was exposed at low tide. (18.525333°N, 72.652008°W).



**Figure 4.14** Coral head (~1.0 m diameter) with living coral at center exposed at low tide at Ca Ira, Léogâne (N18.525333, W72.652008).



**Figure 4.15** Living coral in coral head exposed at low tide at Ca Ira, Léogâne. (N18.525333, W72.652008)



**Figure 4.16.** Water mark for high tides on sea wall at Ca Ira, Léogâne. Residents indicate high tides no longer extend up the wall to the former high tide level (N18.524924, W72.650871)



**Figure 4.17.** Exposed coral head at Ca Ira, Léogâne. Team members measuring uplift of coral head. (N18.525333, W72.652008)

The GEER team also conducted reconnaissance along the coast near L'acul on February 4, where aerial imagery showed additional areas of exposed coral reefs (Figure 4.18). We note that the L'acul site is 0.5 to 0.75 km north of the Enriquillo-Plantain Garden fault zone (EPGFZ) which trends west-northwest to the coast (west of L'acul). Small areas of coral heads were exposed above the water at the time of our visit (Figures 4.19 and 4.20), and the water level apparently was approximately one hour prior to high tide. The team observed a much larger area that apparently is now exposed at low tide, based on the height (3 to 5 cm) of living coral exposed above the water level during our visit and the approximate tidal range of 0.4 to 0.6 m. In general, the amount of uplift estimated at the L'acul site appears to be approximately the same order of magnitude as that observed at Ca Ira. Dr. Mann is working with a team from the U.S. Geological Survey (including Dr. Carol Prentice) to further document and quantify uplift recorded by corals along the coast.

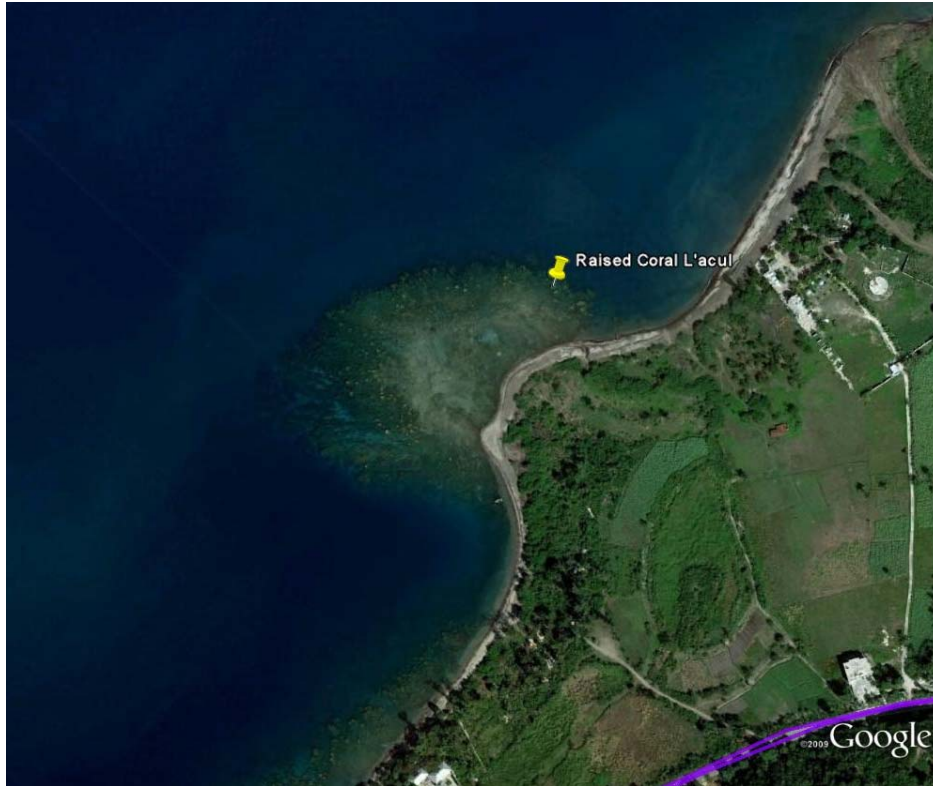


**Figure 4.18** Aerial view of coral uplift near L'acul.  
(See GEER Haiti Report.kmz for location)



**Figure 4.19** GEER team members inspecting uplifted coral reef near L'acul Coral heads are exposed above water at right, approximately one hour prior to high tide. (N18.446463, W72.688354).



**Figure 4.20** Fleshy living, or recently living, coral collected from the top of a coral spire projecting about 3 to 5 cm above water level at the time of the GEER field visit. (N18.446463, W72.688354)

Our reconnaissance indicates that uplift occurred over a minimum distance of about 8 km along coast, extending generally north-northeast between L'acul and Léogâne (See Figure 3.2 in Section 3.0 Regional Geology). The west-southwest trending EPG fault extends offshore in the area just south of L'acul; thus, this area of observed uplift is directly north of the fault. We note that the coastal uplift observed north of the EPG fault in this area is not consistent with the apparent long-term geomorphic expression of south-side up vertical slip on the EPG fault that has uplifted the hills south of the fault.

Our preliminary review of pre- and post-earthquake aerial imagery indicates that the area of coastal uplift may extend north from Ca Ira to Cheridan, and possibly east to near Carrefour. Additional areas of possible coastal uplift were observed along the coast to the west in the area north of Port Royal. In this area, the vertical component of slip is north-side up (hills are north of the fault), which is consistent with the potential uplift observed along the coast north of Port Royal.

The apparent broad region of uplift seems unusual for a well-defined, dominantly strike-slip faulting event. It is possible that broad distributed slip occurred along un-mapped folds or faults north of the EPG fault, as some of the aftershocks, and distal ends of the primary earthquake rupture process, have a component of reverse slip. We understand that Drs. Mann and Koehler are evaluating available industry offshore geophysical data which show a fault with relative uplift on the north in the vicinity of Leogane Point. New offshore geophysical data is planned to be acquired by Woods Hole Marine Laboratory. These existing and new offshore data should help understand the mechanisms responsible for the broad coastal uplift, and also strain partitioning between the EPGFZ and other possible geologic structures.

#### 4.4 Summary

The combined field reconnaissance efforts of three teams as of early February included multiple traverses across the Enriquillo-Plantain Garden fault in areas east and west of the epicenter, and along the entire length of the fault area where aftershocks have been recorded during the three weeks following the 12 January earthquake. Based on the observations of the absence of surface slip on the fault, and combined with the reports from local residents (such as described in the EERI/USGS/GEER reconnaissance report; Eberhard et al., 2010) that no ground deformation has been observed that could be attributed to surface faulting, the GEER team concludes that the EPG fault did not rupture at the surface on-shore, and that no surface faulting occurred onshore on any other faults. No information is available to assess whether displacement may have occurred on the off-shore extent of the EPG fault. However, given that the major moment release in the earthquake occurred at depth onshore and just west of the epicenter, the absence of surface faulting over the high slip portion of the fault plane strongly supports the interpretation that the rupture did not reach the surface onshore or offshore.

A particular issue to resolve in order to fully understand and quantify the earthquake hazard for Port-au-Prince and the surrounding region is whether the January 12 rupture occurred on the EPGFZ or on another fault. While the earthquake does not appear to have caused surface rupture, observations of coastal uplift described in the previous section document that the fault rupture uplifted a broad region (more than 8 km in width) north of the mapped fault. Given that such uplift over a broad region is not expected from a strike-slip earthquake, and based on the modeled component of reverse slip from the earthquake focal mechanism and the slip inversion (as described in Section 2.0, Figure 2.2), it is possible that the fault rupture did not occur on the EPGFZ, and that it occurred on a steeply dipping blind or buried oblique slip fault located north of the EPGFZ. If the EPGFZ did not rupture during the January 12 earthquake, the earthquake hazard for Port-au-Prince and region to the west may be larger than recently estimated by the U.S. Geological Survey (<http://pubs.usgs.gov/of/2010/1019/>). It also is possible that the EPGFZ only ruptures in larger magnitude earthquakes as described in previous seismic hazard assessments ( $M_w$  7.5 to 8.5, Geomatrix Consultants, 2004;  $M$  7.2 or larger, Mann et al., 2008). The absence of surface rupture along the geomorphically well-expressed fault during this large, shallow earthquake raises some concern regarding the ability to capture dependable recurrence estimates for large paleoearthquakes on the basis of paleoseismic trenching. Typically, it would be expected that paleoseismic trenching across a strike slip fault such as the EPGFZ would capture the record of large paleoearthquakes. This earthquake event is an important case study in this regard.

In the near future, additional work to survey land deformation and to document the uplift and subsidence history of the epicentral region is planned by geophysicists from Purdue University (Dr. Eric Calais and colleagues, <http://haitigps.wordpress.com/purdue-geophysicists-in-haiti-conducting-gps-research/>) and geologists from the University of Texas at Austin (Dr. Paul Mann) and the U.S. Geological Survey (Dr. Carol Prentice). These data, along with detailed seismological information collected from recently installed seismic stations in Haiti (Dr. Walter Mooney of the USGS), will provide information and constraints on the earthquake rupture and history of deformation of the region, and in particular will help identify the causative fault for the earthquake. However, detailed mapping and paleoseismic studies of the EPGFZ and possibly other active faults will be necessary to more fully characterize the earthquake hazard for the region near the fault.

## References

- Geomatrix Consultants, Inc., 2004, Seismicity Update, U.S. Department of State, New Embassy Site, Port-au-Prince, Haiti: Report prepared for Wiss, Janney, Elstner Associates, Inc., Emeryville, California.
- Lettis, W.R., Wells, D.L., and Baldwin, J.N., 1997, Empirical observations regarding reverse earthquakes, blind thrust faults, and Quaternary deformation; are blind thrust faults truly blind? *Bulletin of the Seismological Society of America*, v. 87, no. 5, p. 1171-1198
- Eberhard, M., Steven Baldrige, S., Marshall, J., Mooney, W., and Rix, G., 2010, The  $M_w$  7.0 Haiti Earthquake of January 12, 2010: USGS/EERI Advance Reconnaissance Team Team Report, V. 1.0, February 18 ([http://www.eqclearinghouse.org/20100112-haiti/wp-content/uploads/2010/02/USGS\\_EERI\\_HAITI\\_V1.pdf](http://www.eqclearinghouse.org/20100112-haiti/wp-content/uploads/2010/02/USGS_EERI_HAITI_V1.pdf)).
- Mann, P., Demets, C., Prentice, C.S., and Wiggins-Grandison, M., 2008, Enriquillo-Plantain Garden Strike-Slip Fault Zone: A Major Seismic Hazard affecting Dominican Republic, Haiti and Jamaica: 18th Caribbean Geological Conference, Santo Domingo, Dominican Republic ([http://www.ig.utexas.edu/jsg/18\\_cgg/Mann3.htm](http://www.ig.utexas.edu/jsg/18_cgg/Mann3.htm))

## 5.0 DAMAGE PATTERNS

### 5.1 Introduction

Earthquake-induced damage in Port-au-Prince was devastating and widespread. Yet, there were clearly areas of the city where little to no damage occurred, and areas of the city where an overwhelming majority of the buildings were severely damaged or destroyed. These types of damage patterns are common in earthquakes, and a wide number of factors need to be considered in order to conclusively piece together the causes. For a given earthquake, these factors include, but are not limited to: (1) Relative distance from the fault rupture plane, (2) Construction type and quality, (3) Local soil conditions (i.e. strength/stiffness of the foundation soil, depth to bedrock, impedance contrasts, age/geology), (4) Topography (topographic and basin effects), and (5) Near fault effects (rupture directivity, fling step, hanging wall effects, polarity effects, etc.). Often several of these factors work together and it can be difficult to identify the primary cause of damage.

This section primarily attempts to identify damage patterns in Port-au-Prince relative to local soil conditions/geology, topography, and construction type. However, it must be understood that the discussion of construction type is very broad and is based on limited field observations by geotechnical engineers coupled with properties that can be identified from satellite imagery (i.e. density and size of buildings, type of roof, etc.). A detailed ground-based survey by structural engineers in some of these areas would be very valuable in piecing together damage patterns. Additionally, no discussion regarding distance from the fault rupture plane and near fault effects is provided below. Most of the locations in Port-au-Prince are at a relatively similar distance away from the fault (20 – 25 km, Figure 5.1), and due to this distance and the direction of rupture propagation (i.e. away from Port-au-Prince to the west) near fault effects are not expected to have played a role in the damage patterns. However, near fault effects (particularly forward directivity) may have played a strong role in the severe damage observed by the GEER team in Leogane (approximately 30 km due west of Port-au-Prince along the coast, Figure 5.1). Leogane also sits on top of young/soft Quaternary soil deposits, which may have also amplified shaking in this area (see Section 2.0 Regional Geology). Other than these brief observations, Leogane has not been considered in depth in this damage patterns section.

This section investigates, on a limited scale, some of the damage patterns around Port-au-Prince relative to the above mentioned factors. It is based on “boots on the ground” observations made by the GEER team members, as well as a comprehensive building damage assessment performed using satellite and aerial imagery by UNOSAT (United Nations Operational Satellite Applications Programme; <http://unosat.web.cern.ch/unosat/>). The basis of the investigation is heavily weighted toward general categories of structural damage, as this is the most visible manifestation of strong ground shaking in a densely populated area, and was the primary focus of the UNOSAT survey. Other types of damage were observed by the GEER team in and around Port-au-Prince, such as landslides in the foothills heading up to Petion-Ville and foundation, transportation, and lifeline failures due to soil liquefaction in coastal areas. In general, foundation and liquefaction failures seemed to be confined primarily to a limited area of man-made fills and Quaternary alluvial deposits right along Port-au-Prince Bay. Therefore, it appears that these issues did not play a large role in the widespread damage around Port-au-Prince.

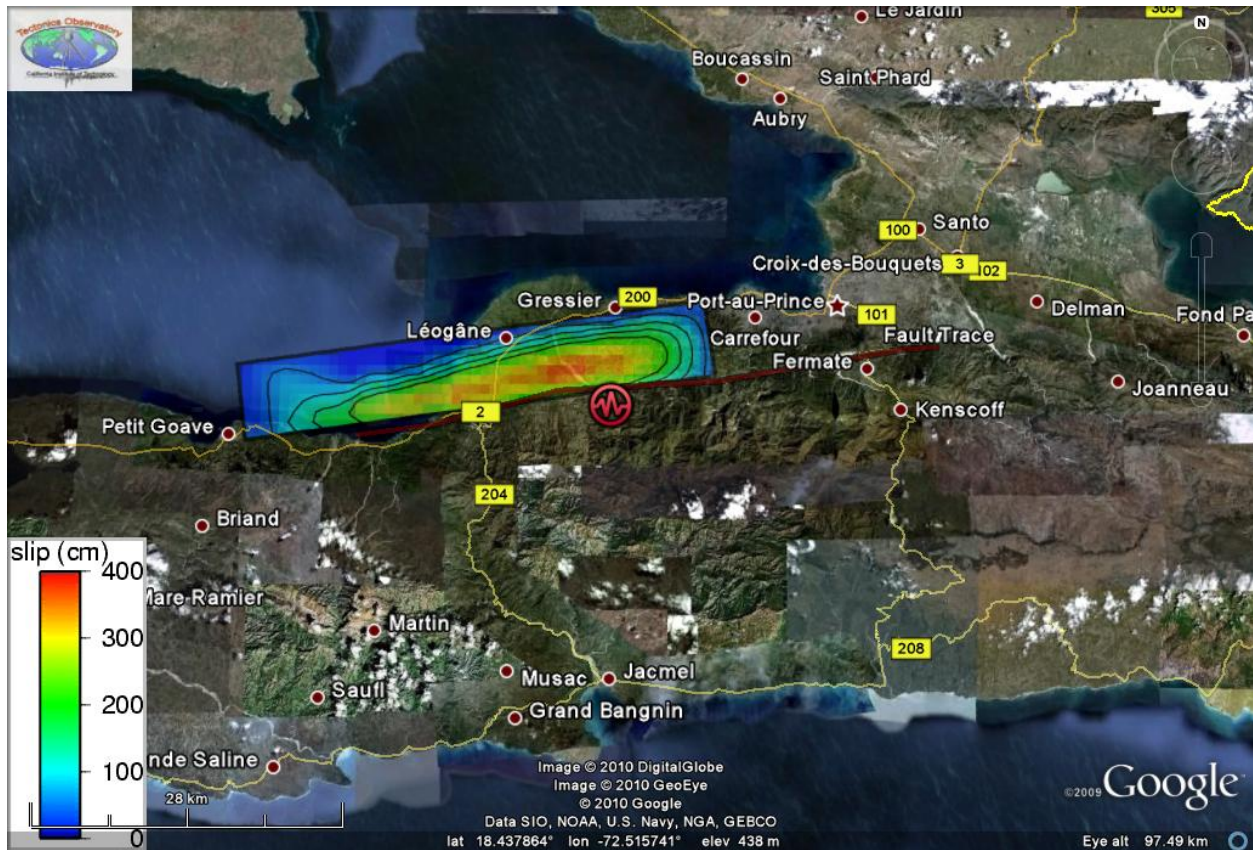


**Figure 5.1** Estimated fault rupture distribution for the 2010 Haiti earthquake ([http://tectonics.caltech.edu/slip\\_history/2010\\_haiti/](http://tectonics.caltech.edu/slip_history/2010_haiti/)) and location of major city centers.

## 5.2 Local Geology and Topography

A 1:250,000 scale geologic map of the region around Port-au-Prince is shown in Figure 5.2. As discussed in Section 2.0 Regional Geology and shown in Figure 5.2, the city of Port-au-Prince is founded on three broad geologic units from youngest to oldest: (1) Quaternary period deposits (not differentiated into Holocene or Pleistocene epoch), (2) Pliocene epoch deposits, and (3) Miocene epoch deposits. Generally, it is expected that the older deposits consist of stiffer, stronger soils/rock. Figure 5.3 is a shaded relief map for a portion of Port-au-Prince derived from a 1-m LIDAR DEM collected by RIT for the Worldbank (<http://ipler.cis.rit.edu/projects/haiti>). Also shown in this figure are the geologic boundaries from a geo-referenced version of the geologic map shown in Figure 5.2. Interestingly, the geologic map indicates that the Pliocene deposits extend almost to the coastline within the central part of the city, yet the topographic data indicate that the flat plain (which presumably corresponds to the Quaternary deposits) extends a significant distance inland. It is more likely that the contact between the Quaternary and Pliocene deposits occurs at the break in slope where the topography steepens, which would indicate that most of the blue areas in Figure 5.3 represent Quaternary sediments. However, this interpretation cannot be verified without further field work.

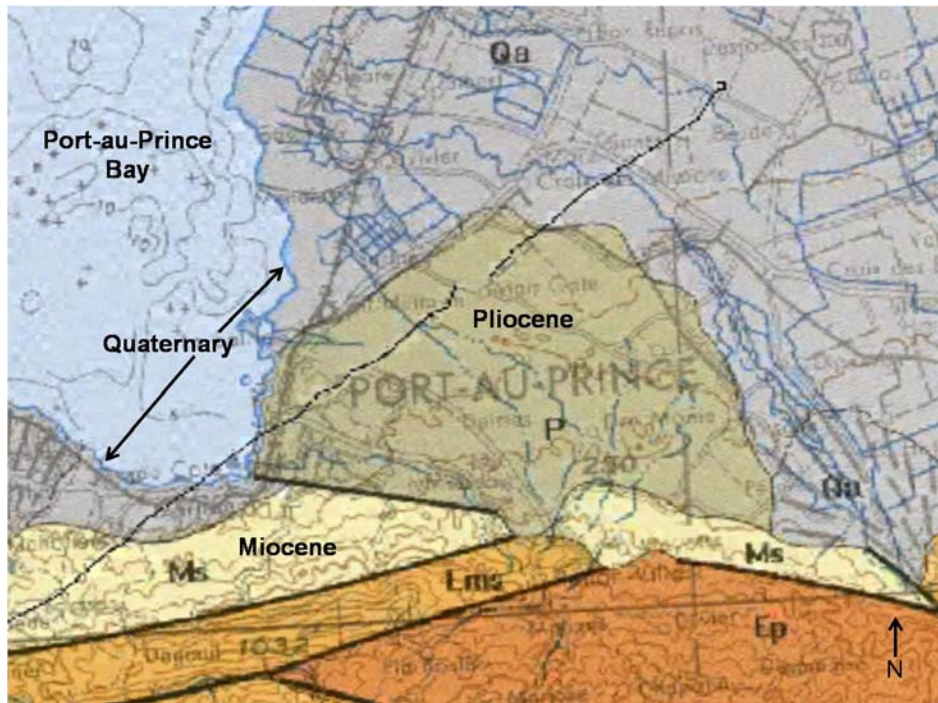


**Figure 5.2** Geology of Port-au-Prince area.  
(C.E.R.C.G. IMAGEO Lambert, Gaudin, and Cohen, 1987)

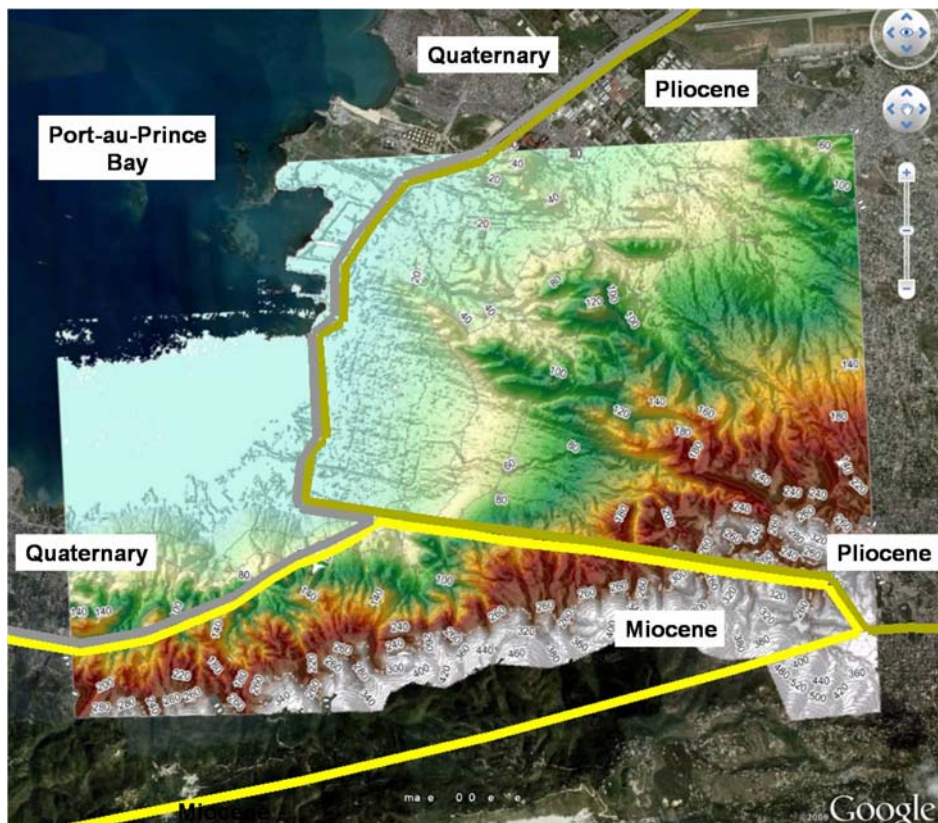


**Figure 5.3** Shaded topographic relief map of the Port-au-Prince area with geologic boundaries from the geologic map shown in Figure 5.2.

### 5.3 UNOSAT Damage Assessment

The UNOSAT damage assessment in Port-au-Prince was a mammoth effort whereby over 90,000 buildings were visually surveyed via post-earthquake satellite and aerial imagery in order to group each structure into one of four categories: (1) Destroyed, (2) Severe Damage, (3) Moderate Damage, and (4) No Visible Damage. The survey also attempted to organize the damage according to classes such as high density built-up zone, low density built-up zone, shanty zone, industrial zone, etc. An example of one of these UNOSAT damage assessment maps is presented in Figure 5.4. The most recent versions of these maps may be found at [http://unosat.web.cern.ch/unosat/asp/prod\\_free.asp?id=52](http://unosat.web.cern.ch/unosat/asp/prod_free.asp?id=52).

The UNOSAT survey basically found that on average 9 – 12% of the 90,000 surveyed buildings were destroyed, 7 – 11% of the buildings were severely damaged, and 5 – 8% of the buildings were moderately damaged. Interestingly, on average, the overall percentage of damaged buildings in shanty zones (~ 28%) was approximately the same as the overall percentage of damaged buildings in high density (~ 30%) and moderate density (~ 27%) built-up zones. This type of work is invaluable to both the humanitarian and scientific communities and will be the basis for many future studies. However, it must also be accepted with some limitations as these types of surveys do not always capture the magnitude of destruction on the ground. As an isolated example, consider the two steel frame warehouses discussed in Section 6.0 Port Facilities and Coastal Infrastructure of this report. Both of these buildings were heavily damaged and will need to be torn down, yet they were classified as No Visible Damage by the UNOSAT survey. This is not meant to criticize the survey, it is only meant to confirm the well understood pattern that damage observed on the ground will typically be greater than the damaged observed from imagery. Therefore, as a lower-bound estimate, one might assume that on average a minimum of 30% of the buildings in Port-au-Prince sustained damage severe enough to be visible from the air. However, certain areas of the city sustained higher percentages of destroyed or severely damaged buildings, while other areas of the city sustained much lower percentages.

A Google Earth (GE) .kmz file was created from the ESRI database compiled by UNOSAT ([www.unosat.org/shared/Haiti-HQ-2010/Data/UNDP\\_UNOSAT\\_v2.zip](http://www.unosat.org/shared/Haiti-HQ-2010/Data/UNDP_UNOSAT_v2.zip)) in order to superimpose GEER team observation and measurement locations, geologic data, and topographic data onto the structural damage observations. The ability to spatially link all of this information is a critical step to understanding damage patterns. The .kmz damage assessment file from the UNOSAT database was created by personnel from CAST (Center for Advanced Spatial Technologies; <http://www.cast.uark.edu/>) after the GEER reconnaissance, and unfortunately was not available to the team in the field. The approximate extents of the UNOSAT survey are superimposed in red on GE imagery in Figure 5.5. Some key landmarks such as the port and airport are also included for reference. Additionally, the GPS track logs for the GEER team (shown in purple) and flag markers identifying areas where Spectral Analysis of Surface Waves (SASW) tests were conducted are also shown. SASW tests were conducted to obtain quantitative evidence of the near surface soil stiffness (i.e. shear wave velocity profiles) in various areas affected by the earthquake. Many SASW surveys were conducted at the port and along the coast west of Port-au-Prince to help assess soil liquefaction damage. However, only a limited number of profiles (three) were conducted in the city due to time constraints and the difficult nature of getting around a heavily damaged city.

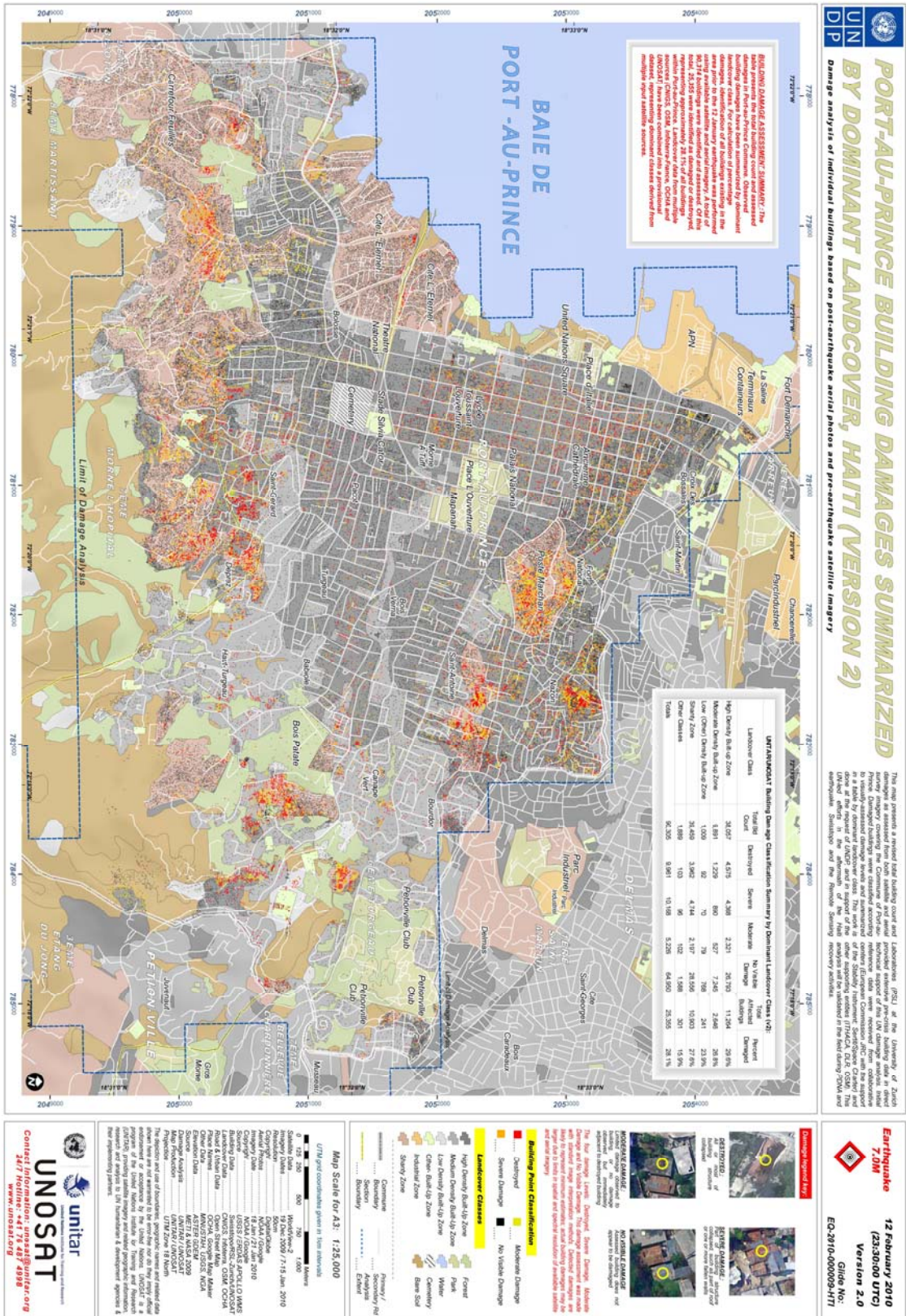
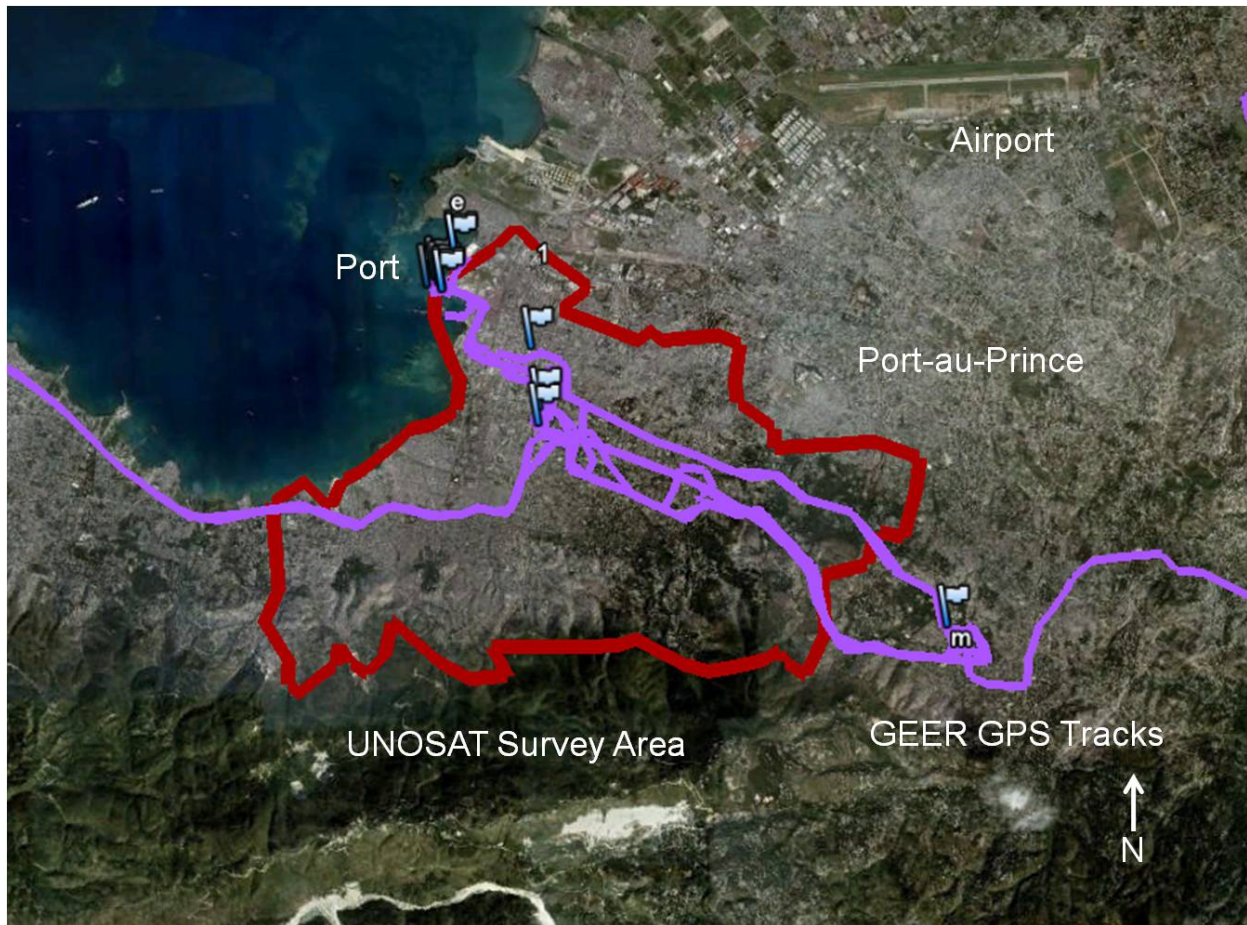


Figure 5.4 UNOSAT building damage assessment map for Port-au-Prince categorized by dominant landcover ([http://unosat.web.cern.ch/unosat/asp/prod\\_free.asp?id=52](http://unosat.web.cern.ch/unosat/asp/prod_free.asp?id=52)).



**Figure 5.5** Approximate area of the UNOSAT damage survey in Port-au-Prince. Also shown are the GEER team GPS track logs and markers identifying locations where SASW testing was conducted.

#### 5.4 Relationship between Damage Patterns and Geology

Figure 5.6 shows the buildings categorized as Destroyed in the UNOSAT survey relative to the Quaternary (Qa), Pliocene (P) and Miocene (Ms) deposits discussed in Section 5.2. It is evident from this broad view that many buildings were destroyed in each of these three deposits (however, recall that the geologic boundaries are somewhat uncertain). However, the picture is skewed somewhat because only the Destroyed buildings are shown (approximately 10,000 points). When one zooms in on the damage, certain patterns begin to emerge. The following discussion will focus on the area boxed in pink in Figure 5.6.

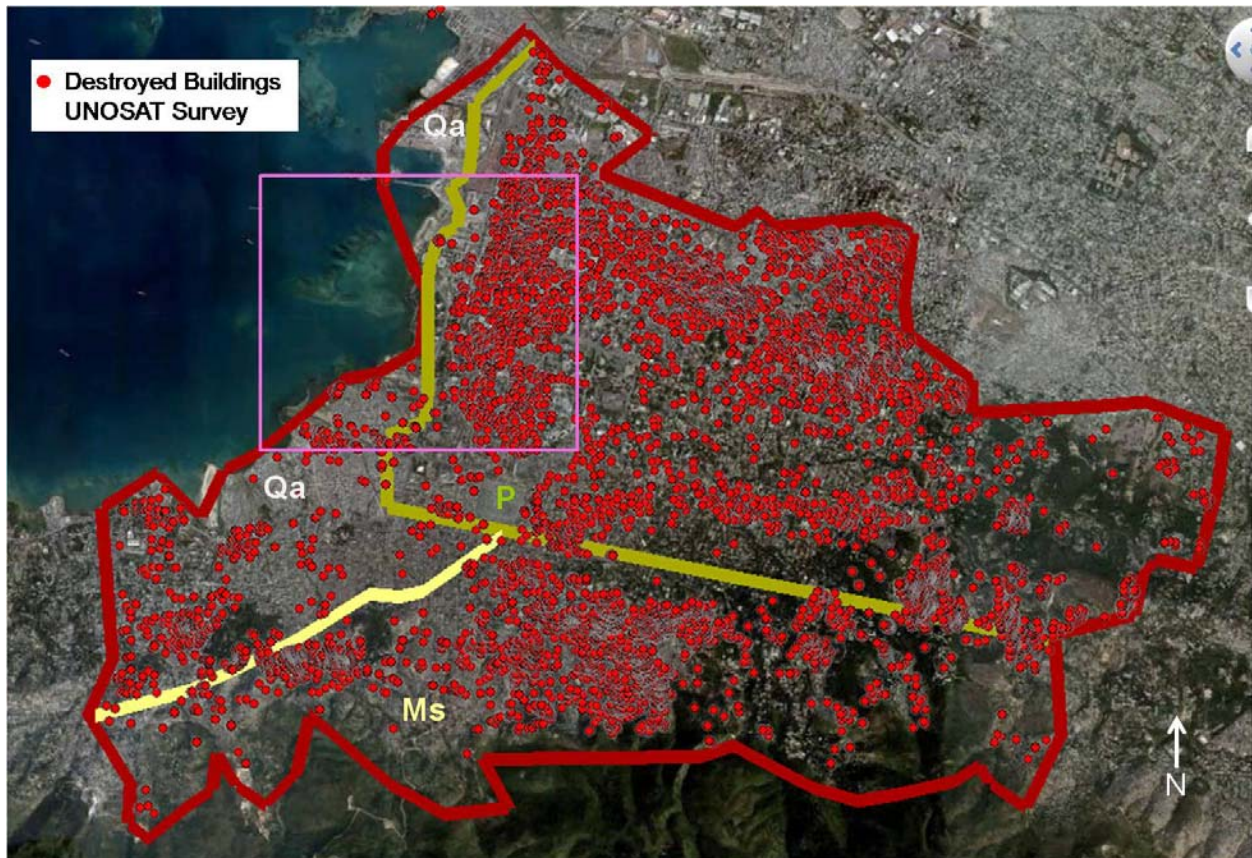


**Figure 5.6** Buildings classified as Destroyed in the UNOSAT survey relative to the three geologic units (Quaternary = Qa, Pliocene = P and Miocene = Ms) underlying the survey area. Note that the destroyed buildings shown in this figure only represent about 10% of the more than 90,000 total buildings categorized in the UNOSAT survey (refer to the text for more detail).

One intensely damaged zone noticed on the GEER reconnaissance was an area located due west and north of the Presidential Palace. This area is boxed in pink in Figure 5.6 and shown in Figure 5.7 along with the buildings that were categorized as either Destroyed (red dots) or No Visible Damage (black dots) in the UNOSAT survey. Also shown are three flag markers where Spectral Analysis of Surface Waves (SASW) testing was performed to investigate the near-surface soil layering and stiffness in the area. It is clear that nearly every building on some of these blocks was completely destroyed (particularly just west and south of SASW 8). However, it is also clear that other areas nearby (e.g. the extreme left-hand bottom corner of Figure 5.7) had very few destroyed buildings. Interestingly, according to the published geologic map, the heavily damaged area lies on Pliocene deposits, while the lightly damaged area lies on younger (presumably softer) Quaternary deposits. However, the revised interpretation of the Quaternary/Pliocene contact (see Section 5.2) would place both of these areas within Quaternary alluvium. One reason for these differences in damage may be building type. Most of the buildings in the heavily damaged zone were larger, multi-story, reinforced concrete structures, while most of the buildings in the lightly damaged area were smaller, densely packed Shanty's with tin roofs (note the difference in density of black dots in the two areas). Several pictures of the type of structures and damage encountered in the heavily damaged zone near SASW 8 are shown in Figure 5.8.

The Presidential Palace also lies on the eastern edge of this heavily damaged zone. The damage to the Presidential Palace (Figure 5.9) was documented by many news crews covering the aftermath of the earthquake due to its symbolism for the widespread, devastating destruction throughout the city. The GEER team conducted two SASW tests (SASW 6 and SASW 7) and one H/V Spectral Ratio test on the grounds of the Presidential Palace. These results have not been fully processed yet, but will be made available as soon as they are complete.



**Figure 5.7** Buildings classified as No Visible Damage and Destroyed in the UNOSAT survey for the boxed area specified in Figure 5.6. Notice the heavily damaged zone lying on P deposits to the north and west of the Presidential Palace and the lightly damaged zone lying on Qa deposits in the lower left-hand corner. Most of the buildings in the heavily damaged zone were larger, multi-story, reinforced concrete structures, while most of the buildings in the lightly damaged area were smaller, densely spaced Shanty's with tin roofs (refer to the text for more detail).



**Figure 5.8** Typical types of structures and damage found within the heavily damaged zone near SASW 8 (N18.550210°, W -72.339638°).



**Figure 5.9** The Presidential Palace lies within the heavily damaged zone noted above. Two SASW tests and one H/V Spectral Ratio test were conducted here (N 18.543633°, W - 72.338905°).

## 5.5 Relationship between Damage Patterns and Topography

Figure 5.10 shows the buildings categorized as Destroyed in the UNOSAT survey relative to a color-shaded topographic map of the Port-au-Prince area. These 20-m, color-shaded contours were generated by personnel from CAST using LiDAR data processed by Chris Crosby at OpenTopography ([http://opentopo.sdsc.edu/files/Haiti/WorldBank\\_Haiti\\_lidar\\_hs\\_v1.kmz](http://opentopo.sdsc.edu/files/Haiti/WorldBank_Haiti_lidar_hs_v1.kmz)). As was the case with the varied geologic deposits shown in Figure 5.6, it is evident that many buildings were destroyed in all types of topography. However, when one zooms in on the damage, certain patterns begin to emerge. The following discussion will focus on the two areas labeled in Figure 5.10.

One interesting area lying on steep topography is shown in Figure 5.11 along with the buildings that were categorized as either Destroyed (red dots) or No Visible Damage (black dots) in the UNOSAT survey. This zone is labeled as Area 1 in Figure 5.10. There is almost a distinct line that could be drawn from east-to-west that separates heavy damage to the south from almost no visible damage to the north. When one zooms in on this area there appears to be no significant difference in the type of structures. All of them appear to be densely packed Shanty-type buildings. It is possible that the steepness of the slope affected this pattern, but no conclusive evidence is known at this time.

Another interesting area lying on a transition from moderate to steep topography is shown in Figure 5.12. This zone is labeled as Area 2 in Figure 5.10. Once again, there is almost a distinct line that can be drawn from east-to-west that separates heavy damage to the south from no visible damage to the north. However, in this case there is both a distinct difference in the type of structure (and likely quality of construction) and type of topography. The structures to the north are larger buildings that appear to be nice homes (some with swimming pools). They are also constructed on more gradual topography. Very few of these homes were damaged. The structures to the south are Shanty-type structures, and the ones that are damaged most severely are located near the top of the hillsides/ridges. This could be evidence of ridge-top focusing of seismic energy. Conversely, the line of Shanty's where no visible damage is noted (bottom center of Figure 5.12) are constructed in a valley.

## 5.6 Conclusions

The observations of damage patterns noted above are just that: isolated observations made from a combination of field information and aerial imagery without rigorous analysis. As discussed at the beginning of this section, there are a wide range of factors that affect damage patterns during earthquakes and many times multiple factors combine to create a complicated mosaic of destruction. However, there is important information to be gained from these damage patterns and there is a wealth of information available for examination from the Haiti earthquake. This pool of information will only continue to grow as more research teams are deployed to the area.

Further investigations regarding damage patterns around Port-au-Prince would benefit greatly from better geologic mapping, local measurements of shear wave velocity profiles throughout the city, structural damage assessments in areas where abrupt changes in the level of destruction were noted, and further investigations of topography such as the direction and angle of slope. The GEER team will continue to conduct more detailed analyses related to this topic.

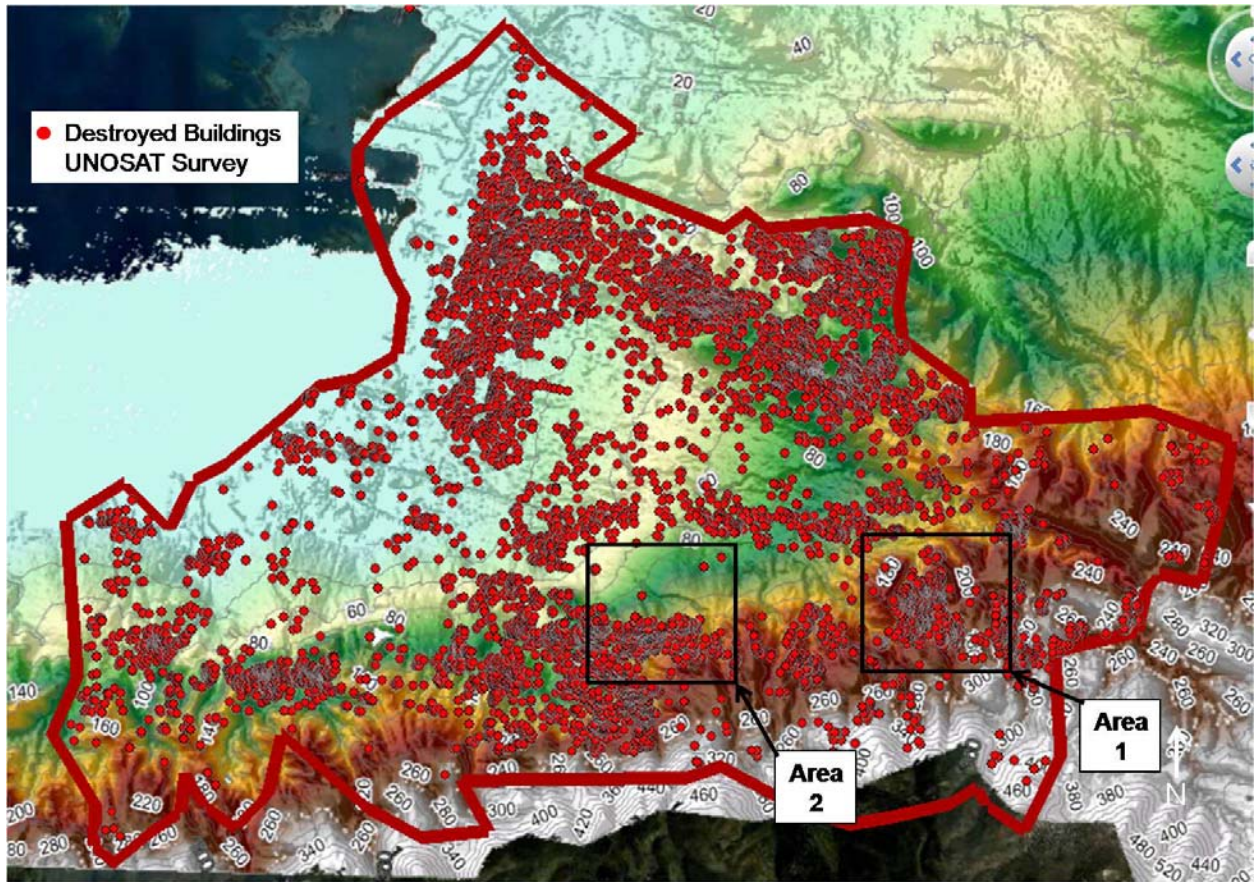


**Figure 5.10** Buildings classified as Destroyed in the UNOSAT survey relative to topography in the Port-au-Prince area. Note that the destroyed buildings shown in this figure only represent about 10% of the more than 90,000 total buildings categorized in the UNOSAT survey (refer to the text for more detail).

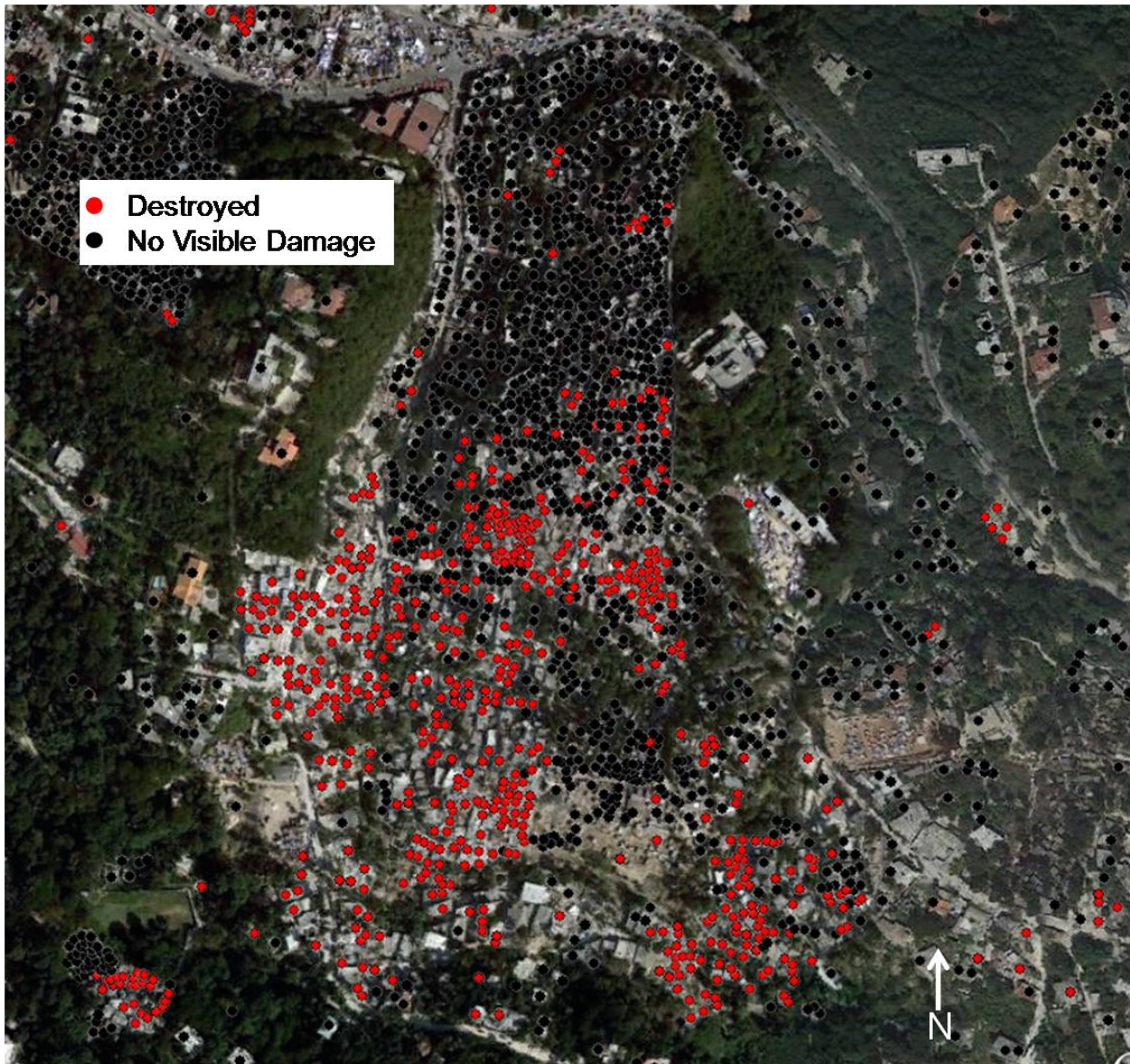


**Figure 5.11** Buildings classified as No Visible Damage and Destroyed in the UNOSAT survey for the boxed area labeled as Area 1 in Figure 5.10. Notice the clear north-south separation between no visible damage and destroyed buildings that bisects the ridgeline east-to-west. All of these buildings appear to be Shanty-type structures with similar construction (refer to the text for more detail).

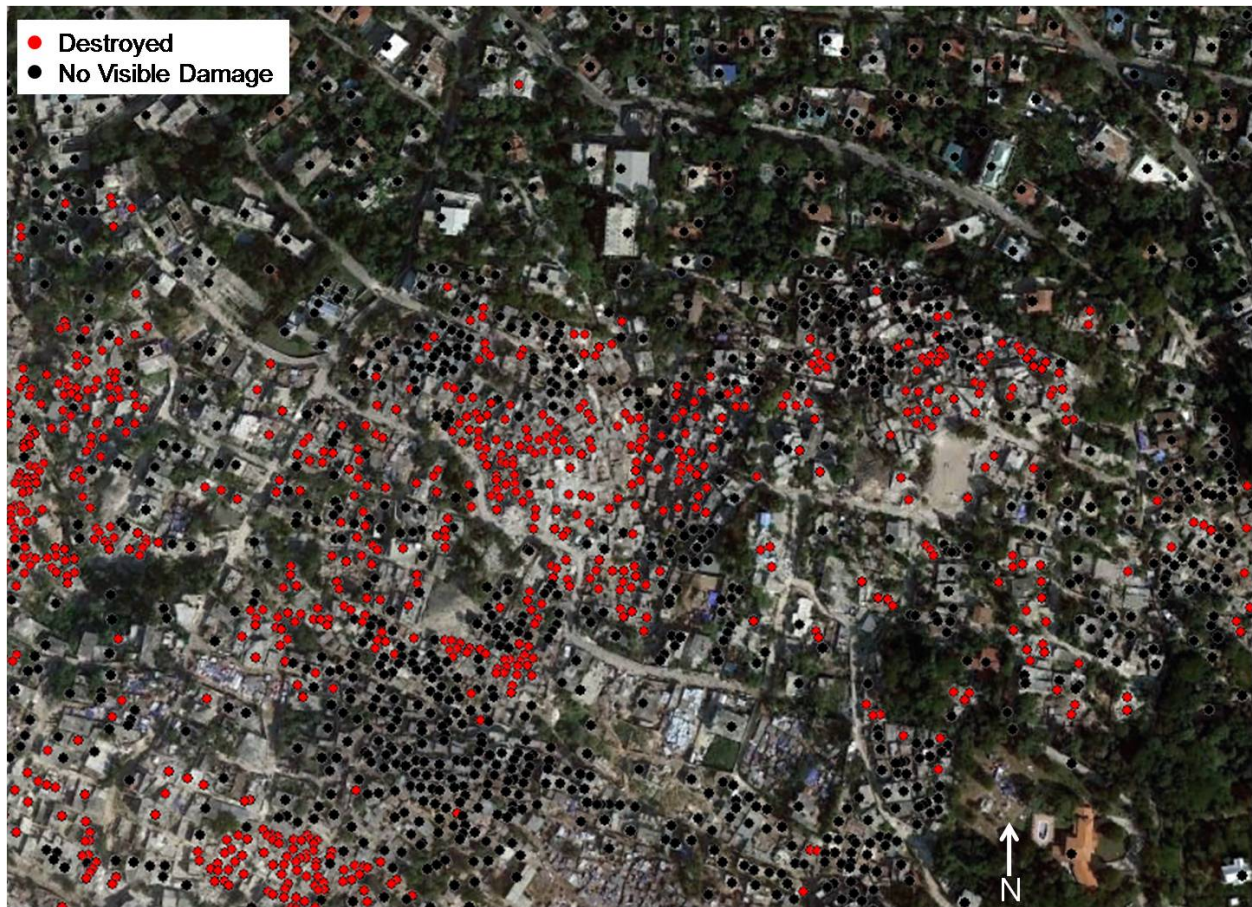


**Figure 5.12:** Buildings classified as No Visible Damage and Destroyed in the UNOSAT survey for the boxed area labeled as “Area for Fig. 10” in Figure 3.8. Notice the clear north-south separation between no visible damage and destroyed buildings that bisects this area from east-to-west. The undamaged buildings to the north are larger homes that appear to be well constructed. Furthermore, they also sit on more moderate topography. The destroyed buildings appear to be Shanty-type structures that sit near the top of the hillsides/ridges (refer to the text for more detail).

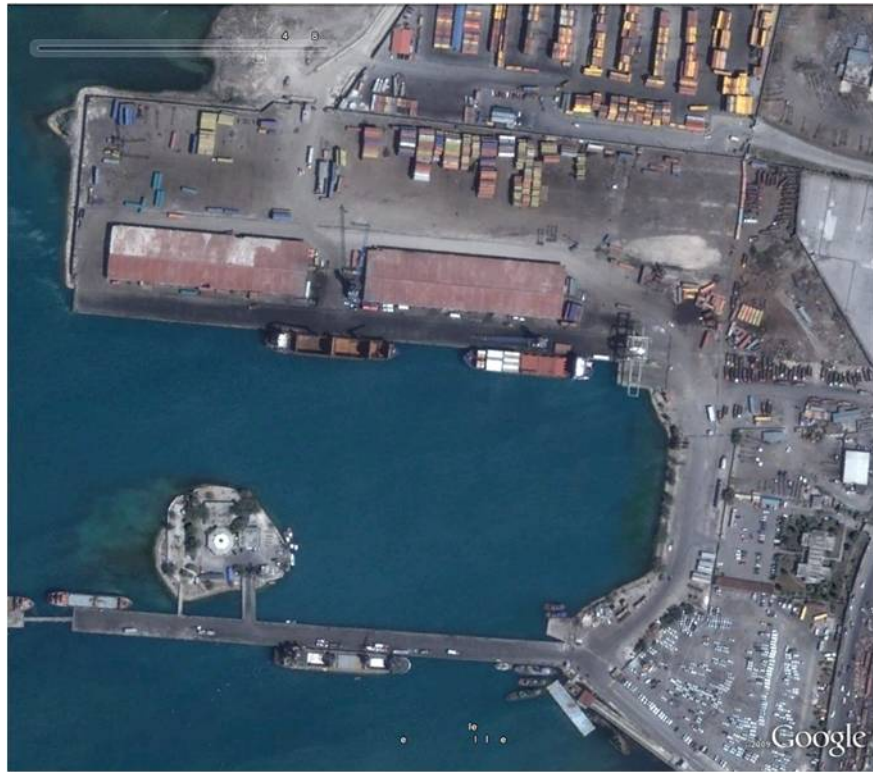
## 6.0 PORT FACILITIES AND COASTAL INFRASTRUCTURE

The main port in Port-au-Prince is operated by the Autorite Portuaire Nationale (APN) and consists of two separate facilities designated as the North Wharf and South Pier. According to data provided by APN, the port handled 978,575 metric tons of cargo in 2005-2006 from 490 ship calls. The port is located slightly north of the main city center of Port-au-Prince and approximately 20 to 25 km from the fault rupture of the 12 January 2010 earthquake (Figure 6.1).

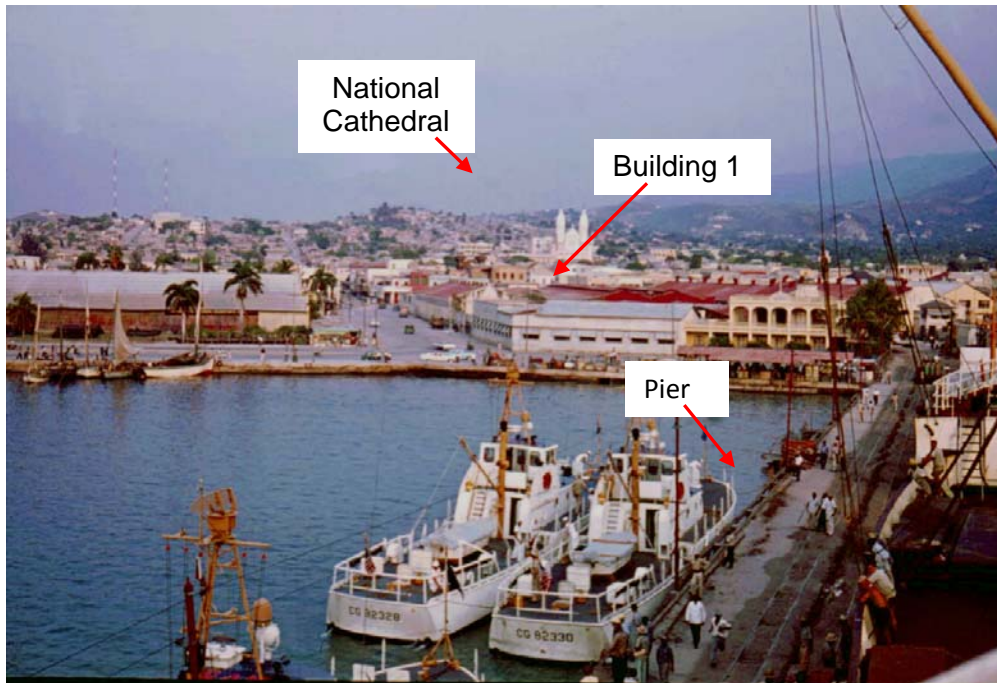
Pre- and post-earthquake aerial images of the port are shown in Figure 6.2, and these images clearly show evidence of liquefaction and lateral spreading, failure of the North Wharf, and collapse of portions of the South Pier. The photo of the port shown in Figure 6.3 (unknown photographer) is circa 1962, and shows one long pier that extends from the main coastal road. This pier is located along the southern margin of the current port (Figure 6.4), which suggests that the present port facility is constructed on fill, likely un-engineered and of unknown origin. Also, from field reconnaissance, it is clear that the fill material extends to the North (to the left and out of view of the photo shown in Figure 6.3), demarcated by dashed lines in Figure 6.4. The port suffered extensive damage during the earthquake (Figure 6.5), inhibiting the delivery of relief supplies to areas affected by the earthquake. Light-colored areas on the ground surface in Figure 6.4 are sand boils/ejecta and can be seen in the eastern half of the container storage yard and behind and between the two warehouses. The locations where large lateral spreading fissures were observed are also shown in Figure 6.5.



Figure 6.1 Location of main port in Port-au-Prince.



**Figure 6.2** Pre- and post-earthquake satellite/aerial imagery (top and bottom, respectively) of the port at Port-au-Prince, Haiti (N18.555058°, W72.351144°). Imagery courtesy of Google Earth.



**Figure 6.3** Photograph of the port circa 1962 (Source unknown).

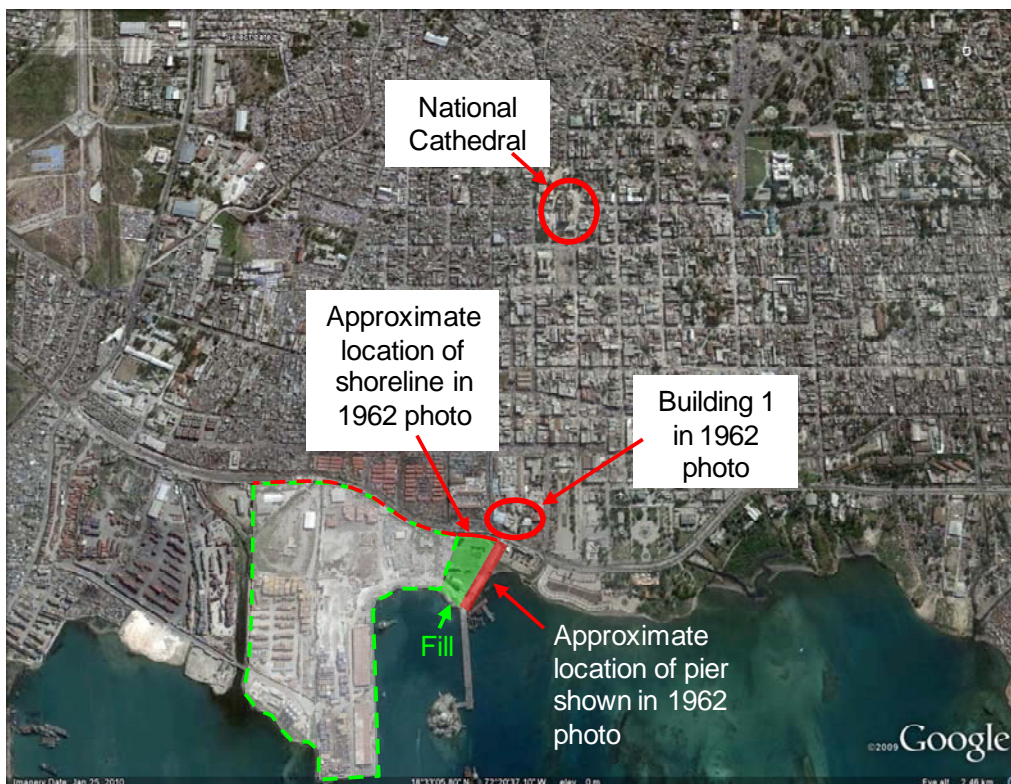


**Figure 6.4** Recent aerial image of port, with the landmarks shown in Figure 6.2 annotated. The extent of the fill to the North (left) is unknown and is thus annotated by dashed lines. Imagery courtesy of Google Earth.



**Figure 6.5** Annotated aerial image of Port de Port-au-Prince showing locations of damage due to the earthquake. Imagery courtesy of Google Earth. (N18.555058°, W72.351144°)

The North Wharf consisted of a pile-supported marginal wharf that was approximately 450 m in length and 20 m in width and was likely constructed on un-engineered fill. The water depth is 8 to 10 m. Other information about the construction of the wharf such as when it was constructed and the number and size of piles is unknown at present. Immediately adjacent to the wharf are two steel-frame warehouses, each approximately 150 m by 40 m. Behind the warehouses is a container storage yard with a large number of mostly empty containers stacked two to four high at the time of the earthquake. There are three cranes at the North Wharf, including one 15-m gauge, A-frame container crane and two rubber-tired mobile cranes.

The North Wharf collapsed, most likely due to liquefaction-induced lateral spreading. Numerous surface manifestations of liquefaction and lateral spreading were present in the vicinity of the North Wharf. By the time the GEER Team arrived at the port (G. Rix on 27 January and 2 February for the rest of the team), the US Navy construction teams had already placed fill over large portions of the road that ran adjacent (on the North side) to the warehouses. The Navy construction workers told the GEER Team that the fill was needed because the lateral spread cracks made the road impassable by vehicles. The presence of these cracks was confirmed by post-earthquake satellite/aerial imagery taken between 13 and 21 January, and re-grading had removed them by the time a 25 January image was taken. Nonetheless, numerous manifestations of liquefaction and lateral spreading were untouched at the time of the GEER Team's inspection (Figures 6.6 through 6.11).



**Figure 6.6** Lateral spreading adjacent to the collapsed North wharf. Note the crane in the water in the background and the metal warehouses on the right. (N18.55622, W72.34787)



**Figure 6.7** Lateral spreading between the two metal warehouses, adjacent to the collapsed North wharf (left). A cumulative total of 89 cm of horizontal movement (determined by crack width) was measured in a zone extending inland approximately 30 m from the post-earthquake shoreline. Post-earthquake imagery indicates lateral spread cracking extended 50 m inland. (N18.556696, W72.34787)



**Figure 6.8** Lateral spreading west of the two metal warehouses. Photo taken facing north with the metal warehouses to the right. (N18.557075, W72.352045)



**Figure 6.9** Lateral spreading west of the two metal warehouses. Photo taken facing south with the metal warehouses to the left. (N18.557075, W72.352045)



**Figure 6.10** Liquefaction and lateral spreading adjacent to the north side of the metal warehouses. Photo on top taken facing west, photo on bottom taken facing east. (N18.556961, W72.349751)

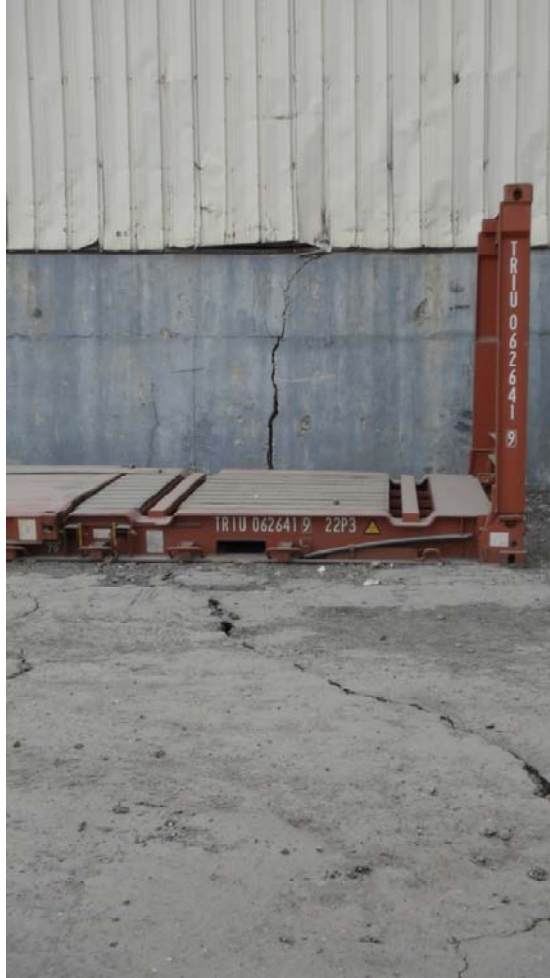


**Figure 6.11** Lateral spreading crack extending into the western foundation wall of the west warehouse. Photo taken facing east. (N18.55721, W72.35179)

Two of the three cranes were apparently on the North Wharf at the time of the earthquake and are now partially submerged. Figure 6.12 shows the A-frame container crane in the foreground and a submerged mobile crane in the background. There was no obvious structural damage to the container crane. Interestingly, a photo taken by an unknown photographer (apparently aboard a ship docked at the eastern end of the wharf) immediately after the earthquake (Figure 6.13) shows that the landside legs of the A-frame crane were still above water, with the crane in its most eastwardly position. However, a U.S. Coast Guard photo taken during an overflight of the port at mid-day on January 13, 2010 shows the crane in the same position as in Figure 6.12 (i.e., moved westward about 60 m from its position in Figure 6.13) and with the base of the crane fully submerged. Also, the January 13 photo shows that additional subsidence occurred at the eastern end of North Wharf (i.e., the location of the crane in Figure 6.12). The National Earthquake Information Center reports no fewer than 45 aftershocks ranging from  $M_w$  4.0 to 6.0 following the main shock until 1:54 pm EST on January 13, 2010. This raises the likelihood that a portion of the observed permanent displacements caused by liquefaction occurred as a result of aftershocks. The second mobile crane was parked between the two warehouses and appears to be undamaged.



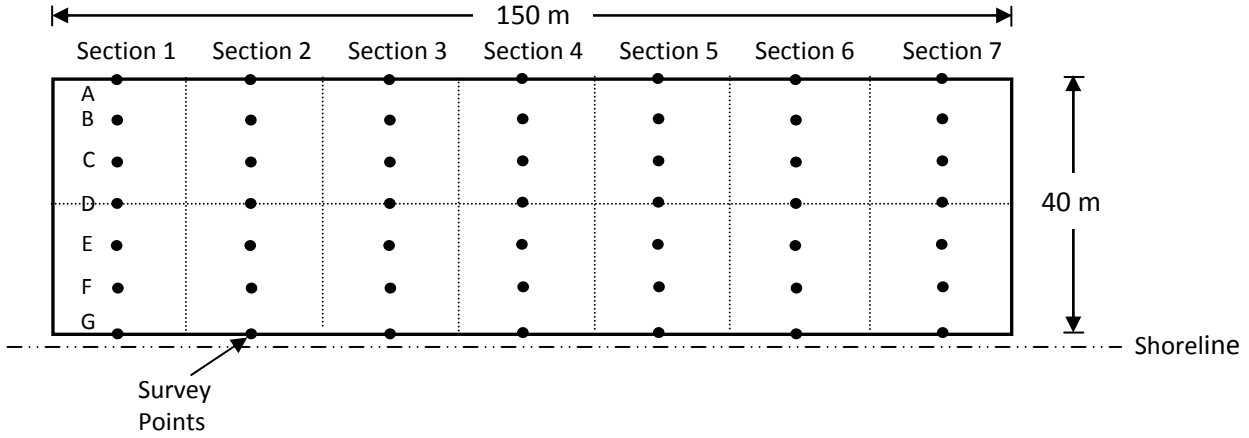
**Figure 6.12** Submerged 15-m gauge container crane (foreground) and mobile crane (background). Photo taken facing west. (N18.55598, W72.348564)



**Figure 6.13** Photo taken immediately after the earthquake with the crane in its most eastward position and with the landside legs of the crane above water. Photo taken facing east. Source: unknown (N 18.556056, W72.347981)

The warehouses suffered severe damage as a result of the lateral spreading and settlement, and will likely have to be torn down. As shown in Figure 6.11, lateral spreading cracks running in the East-West direction cut through each warehouse foundation wall. A detailed survey of the relative elevations and lateral movements of the west warehouse slab is shown in Figure 6.14. The interior slab consisted of 14 separate slabs, two abreast and seven long. Due to lateral spreading, the south wall (adjacent to the shoreline) moved approximately 0.7 to 1.4 m laterally towards the shoreline (i.e., the width of the warehouses increased). The relative elevations across the slab are more difficult to interpret because it was clear that the slab was constructed with a significant slope and/or curvature towards the seaward edge. Without knowledge of the relative elevation differences before the earthquake, these movements cannot be converted to relative settlements due to liquefaction. Nonetheless, the relative elevations across the interior were variable, with the some areas almost 1 m lower than others. It appeared that the

warehouses were founded on strip footings around their perimeters, which settled significantly. Settlements measured at the inland corners of the warehouses are also shown in Figure 6.14. The west warehouse appears to have settled approximately 15 cm relative to the ground surface, while the east warehouse settled more than 40 cm



|   | Survey Pt | Section 1 | Section 2 | Section 3 | Section 4 | Section 5 | Section 6 | Section 7 |
|---|-----------|-----------|-----------|-----------|-----------|-----------|-----------|-----------|
| Vertical Settlement (cm)                      | A         | 0.0       | -6.1      | 27.5      | 42.7      | -7.6      | 32.0      | -4.6      |
|   | B         | -7.3      | -4.3      | -2.7      | 24.7      | -14.9     | 24.7      | -5.8      |
|   | C         | -20.4     | -20.4     | -25.0     | -32.6     | -23.5     | -43.3     | -0.6      |
|   | D         | -24.4     | -18.3     | -21.4     | -2.7      | -13.7     | -47.3     | 0.0       |
|   | E         | -6.7      | -32.6     | -8.2      | -11.3     | -5.2      | -23.5     | -15.9     |
|   | F         | -16.5     | -25.6     | -25.6     | -34.8     | -19.5     | -27.1     | -25.3     |
|   | G         | -48.8     | -63.4     | -74.7     | -79.3     | -67.1     | ?         | -58.0     |
| Displacement of south wall towards south (cm) |           | 71.1      | 94.9      | 119.9     | 104.6     | 141.5     | 131.8     | 84.8      |

\* Assumed datum at north edge of Section 1. All data based on survey with hand level with values adjusted to correct for apparent instrument bias

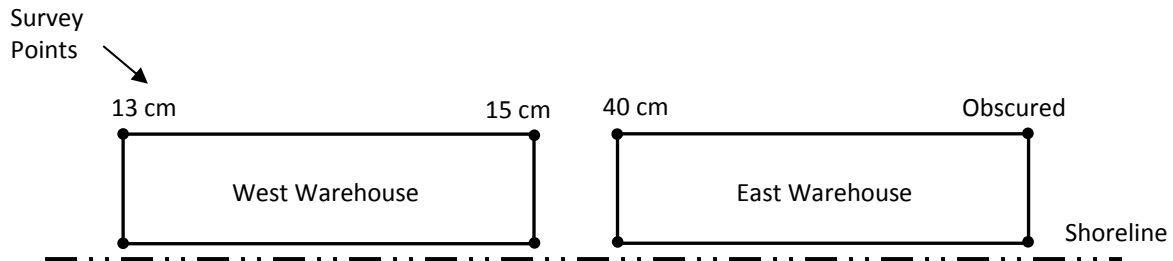


**Figure 6.14** Results of a detailed survey of the relative settlements of the west warehouse slab, and the total settlements at the inland corners of the warehouses

The South Pier is a pile-supported structure that was originally 380 m in length and 18 m in width (Figure 6.5). A large bridge and a small pedestrian bridge that are approximately perpendicular to the longitudinal axis of the pier connected the pier to an island where the port security office is located. The western end of the pier was also connected to three dolphins by small pedestrian bridges. All of the bridges were also pile-supported structures. It is believed that an American or British contractor constructed the pier around 1975. The piles supporting the pier are approximately 51-cm square concrete piles on 4.3 to 4.9-m centers and include both vertical and battered piles. The pile bents are 1.5 m deep and 0.9 m wide and the deck is 45 cm thick (Brian Crowder, personal communication).

During the earthquake, the western-most 120 m of the South Pier and portions of the pedestrian bridges linking the dolphins collapsed and are now submerged. One hypothesis is that the abutment of the pier and the large bridge connecting the pier to the island together provided sufficient lateral restraint to prevent this portion of the pier from also collapsing. Nonetheless, the portion of the pier that is still standing was heavily damaged. US Army divers inspected the piles following the earthquake to determine whether the pier could support loads imposed by trucks carrying relief supplies. They found that approximately 40% of the piles were broken, 45% were moderately damaged, and 15% were slightly damaged. Generally, the batter piles were more heavily damaged than the vertical piles. An aftershock on January 26, 2010 may have caused more damage, and the pier remained closed to traffic as of February 1, 2010. Engineers from U.S. Naval Facilities Engineering Command have developed a strategy that they hope will allow them to repair the damaged in about 10 weeks from the start of construction.

In addition to the damage to the piles supporting the South Pier, the abutment also experienced liquefaction-induced lateral and vertical displacements. Approximately 1 m of fill was required to re-level the approach to the pier as shown in Figure 6.15. Also, the piles supporting the small pedestrian bridge connecting the South Pier to the island could be readily observed. Figure 6.16 shows the damage to these piles, including the extensive damage to the landward row of piles.

North of the main port facility along the shoreline, there were six steel grain hopper silos and two storage yards (Figure 6.17). From aerial imagery, it was determined that the grain silos were built sometime between March 2008 and January 2010. As shown in Figure 6.18, lateral spreading occurred behind the silos (westward side), but the silos and their foundation system showed no visible signs of distress (Figures 6.18 and 6.19). The amount of grain in the silos at the time of the earthquake is unknown. Also, the foundation system for the silos is unknown at this time. Extensive lateral spreading occurred in the two storage yards that are just north of the silos (Figures 6.20 through 6.24). Approximately 2.4 m of cumulative lateral displacement was measured at the northern storage yard. A unique feature of these lateral spreads is that the fill is garbage overlain by cobbly soil (Figure 6.24). However, it is believed that sand underlying the garbage fill liquefied and caused the lateral spreading.

Finally, one of the main entrance roads to the port was heavily damaged by liquefaction-induced lateral spreading, as shown in Figure 6.25.



**Figure 6.15** Approach to the South Pier immediately after the earthquake (top photo: Source unknown; photo taken facing South-East) and after approximately 1 m of fill was placed (bottom photo: photo taken facing West). (N18.554028, W72.348658)



**Figure 6.16:** (top) Damage to piles supporting the pedestrian bridge connecting the South Pier to the island (photo taken facing South) and (bottom) extensive damage to the landward row of piles (photo taken facing West) (N18.554628, W72.351492)

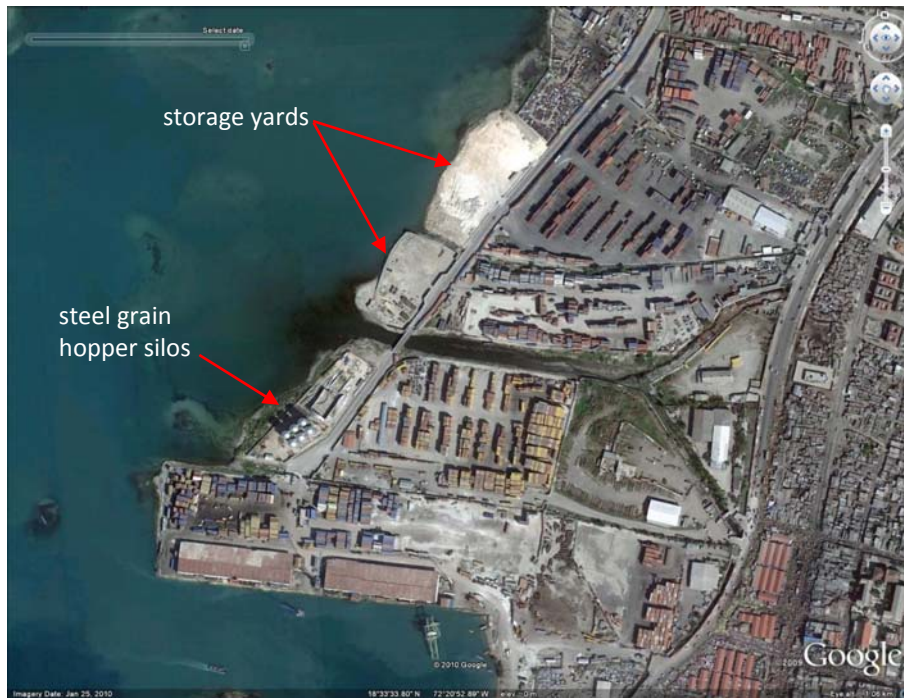
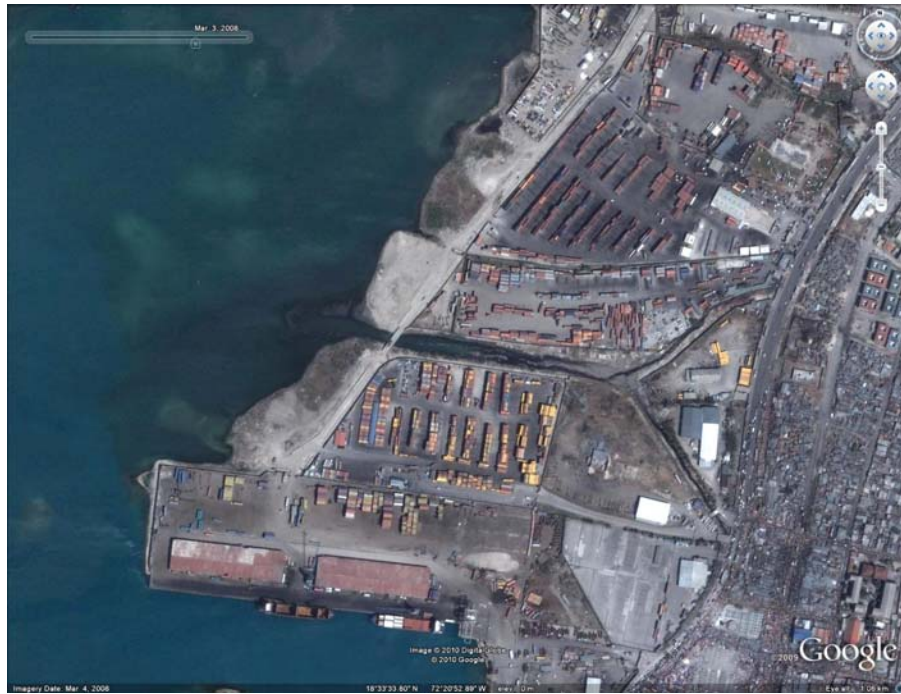


**Figure 6.17** Aerial imagery of the northern part of the port facilities before the steel grain hopper silos and storage yards were built (top: image from March 2008) and after (bottom: image from January 2010). Imagery courtesy of Google Earth.)



**Figure 6.18** Lateral spreading behind (westward side) steel grain hopper silos. However, the foundation system for the silos showed no visible signs of distress.  
Imagery courtesy of Google Earth.



**Figure 6.19** Post-earthquake photo of steel grain hopper silos (photo taken facing North). The silos showed no visible signs of distress.  
(N18.558431, W72.350350)



**Figure 6.20** Lateral spreading in the storage yards in the northern part of the port facility. Imagery courtesy of Google Earth. ( $18^{\circ}33'40.23''\text{N}$   $72^{\circ}20'52.33''\text{W}$ )



**Figure 6.21** Lateral spreading in the storage yards in the northern part of the port facility. Photo taken facing South. ( $18^{\circ}33'41.39''\text{N}$   $72^{\circ}20'52.51''\text{W}$ )



**Figure 6.22** Lateral spreading in the storage yards in the northern part of the port facility. Photo taken facing South. (18°33'41.76"N 72°20'52.25"W)



**Figure 6.23** Lateral spreading in the storage yards in the northern part of the port facility. Lateral spread crack passes through a stone/masonry wall. Photo taken facing South. (Approximate long. and lat. of photo: 18°33'35.15"N 72°20'56.18"W)



**Figure 6.24** Lateral spreading in the storage yards in the northern part of the port facility. A unique feature of this lateral spread is that the fill is garbage. However, it is believed that the liquefaction of the sand below garbage is the cause of the lateral spreading. Photo taken facing North-East. (Approximate long. and lat. of photo: 18°33'38.93"N 72°20'54.89"W)



**Figure 6.25:** Damage to entrance road caused by lateral spreading. Photo taken facing South-East. (Approximate long. and lat. of photo: 18°33'11.61"N 72°20'52.50"W)

To identify the depth(s) and thickness(es) of the soil layer(s) that liquefied at the port, Spectral Analysis of Surface Waves (SASW) and Dynamic Cone Penetrometer Test (DCPT) tests were performed at various locations. All the tests were conducted on Monday, February 1, 2010. The test locations are shown in Figure 6.26, with the latitude and longitude coordinates for each provided in Tables 6.1 and 6.2 for the SASW and DCPT, respectively. Photos of the test setups are shown in Figures 6.27 and 6.28.

The SASW and DCPT results are currently being processed. The SASW results will give the shear wave velocity ( $V_s$ ) profiles at each array location. It is expected that these  $V_s$  profiles will extend to an approximate depth of 6 m based on the range of wavelengths/frequencies collected in the field. If a heavier/lower-frequency source had been available, the depth of these profiles could have been extended significantly. The DCPT were performed to depths ranging from 3 to 6 m until refusal. However, from visual inspection of the free face of one of the lateral spread features (Figure 6.29), the soil profile consists of approximately 10 cm of asphalt on top of 28 cm of well-graded gravel (GW) base, which overlays 30 cm of cobbles. The cobbles are underlain by more GW, the thickness of which could not be ascertained. The depth of the water table is controlled by the tide and appeared to average approximately 1.2 m below the ground surface.



**Figure 6.26** Spectral Analysis of Surface Waves (SASW) and Dynamic Cone Penetrometer Test (DCPT) locations at the port in Port-au-Prince Haiti. Imagery courtesy of Google Earth. (Approximate long. and lat. of center of image: 18°33'27.09"N 72°21'03.51"W)

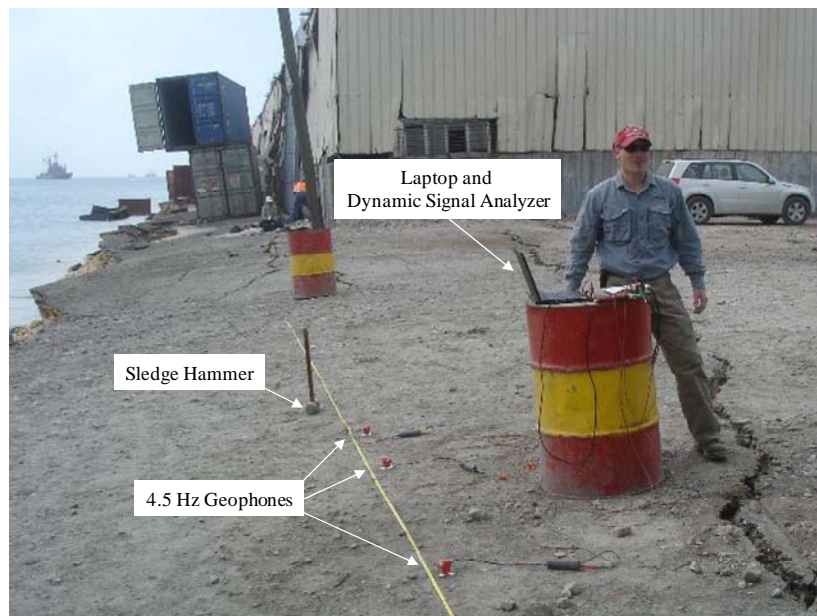


**Figure 6.27** Lightweight, dynamic equipment used to conduct SASW testing in Haiti. This photograph was taken at the location of SASW 1, facing West. (N18.556635°, W -72.350202°).



**Figure 6.28** Dynamic Cone Penetrometer Test (DCPT). This photograph was taken at the location of DCPT1, facing East. (N18.556681°, W -72.350398°).



**Figure 6.29** Near-surface soil layering at the wharf as observed on the free-face of the lateral spread that collapsed the wharf deck. This picture was taken just south of SASW 1 (refer to Figure 6.26), facing East. (N18.556635°, W 72.350202°).

**Table 6.1** Spectral Analysis of Surface Waves (SASW) array locations at the port in Port-au-Prince, Haiti

| SASW Locations at the Port in Port-au-Prince, Haiti |            |             |
|---|------------|-------------|
| Array   | Latitude   | Longitude   |
| SASW 1  | 18.556635° | -72.350202° |
| SASW 2  | 18.556858° | -72.350238° |
| SASW 3  | 18.557468° | -72.350657° |
| SASW 4  | 18.558007° | -72.351057° |
| SASW 5  | 18.557238° | -72.351896° |

**Table 6.2** Dynamic Cone Penetrometer Test (DCPT) sounding locations at the port in Port-au-Prince, Haiti

| DCPT Locations at the Port in Port-au-Prince, Haiti |            |             |
|---|------------|-------------|
| Sounding  | Latitude   | Longitude   |
| DCPT 1  | 18.556681° | -72.350398° |
| DCPT 2  | 18.556983° | -72.349906° |
| DCPT 3/4  | 18.558030° | -72.351066° |

## 7.0 LIQUEFACTION AND LATERAL SPREADING

### 7.1 Introduction

Liquefaction is the process of porewater pressure increase and concurrent loss of strength and stiffness resulting from rapid loading of loose to medium dense cohesionless soils. Earthquake-induced liquefaction and lateral spreading occurred extensively along the coastline around Port-au-Prince Bay and inland along several rivers and streams, and was responsible for the severe damage at the Port au Prince port. The damage to the port is discussed in Section 6.0 Port Facilities and Coastal Infrastructure, while this section focuses on all other locations of liquefaction.

### 7.2 General Observations

Prior to arrival in Haiti, GEER team members identified numerous potential liquefaction-induced failures near the coastline, as shown in Figure 7.1. Potential liquefaction-induced failures were identified up to 38 km from the epicenter and up to 26 km from the fault trace. These data plot well within the boundaries for most distal liquefaction sites proposed by Ambraseys (1988) using worldwide data (Figure 7.2). As discussed by Olson et al. (2005), this suggests that the natural coastal and alluvial soils near Port-au-Prince Bay are only moderately susceptible to liquefaction, although liquefiable Quaternary sediments were generally noted only within short distances from the coast. Additionally, without any strong motion recordings from this event, the level and duration of shaking is unknown. The slip inversions for the event (see Section 2.0 Seismological Aspects) indicate that most of the earthquake energy was released in 6 to 8 seconds, which is relatively short for a M 7 earthquake. This short duration of shaking would have limited the number of cycles of loading and minimized the zones that experienced liquefaction.

Generally, observed liquefaction-induced failures occurred either in fill soils placed to reclaim land for urban areas (e.g., Port-au-Prince port) or in Holocene-active delta fan lobes in coastal areas near the mouths of streams emptying into Port-au-Prince Bay. The most susceptible deposits and largest lateral spreads occurred within active Holocene delta fan lobes between Petite Goave and L'acul where well-defined deltas exist where local streams discharge from a mountain front near the coast. The short distance between the mountain front and coast has not allowed significant sorting and grain size reduction in the delta lobes, such that the sediments consist predominantly layers of coarse to fine, sand and silty sand. In these areas, the alluvial soils may have been deposited in a relatively loose state prior to being potentially densified by wave action. Further inland, liquefaction features were limited to the floodplains of lower-gradient, meandering streams occasionally found north and east of Port au Prince. Most of the streams along the southern rim of Port au Prince Bay are high-gradient, braided ephemeral streams that carry coarser sediment loads. Almost no liquefaction features were identified along these streams inland of the coastline. In the city of Port au Prince, most of the streams are rather shallow and ephemeral, and have been channelized and often lined with stones or concrete. As a result, liquefaction was unlikely to occur in these drainage channels. Furthermore, nearly all of the drainage channels became clogged with debris and trash following the earthquake. This precluded the team from identifying any potential liquefaction features using aerial photography or direct observation.

During the reconnaissance mission, the GEER team performed more detailed investigations of five potential liquefaction sites, namely the Port-au-Prince port, the coastal area north of the port, a coastal site near the village of L'acul, a coastal site near the village of Fouche, and a

coastal site near the village of Grand Goève. The failures at the port and at the coastal area immediately north of the port are described in Section 6.0 of this report. The soils involved in these failures consisted of clean calcareous fill sands, likely placed by end-dumping. The remainder of this section focuses on the coastal failures involving natural sand deposits.



**Figure 7.1.** Potential liquefaction, lateral spreading, and coastal failure sites identified from post-earthquake aerial photography (sites identified as open hexagons). Imagery courtesy of Google Earth.

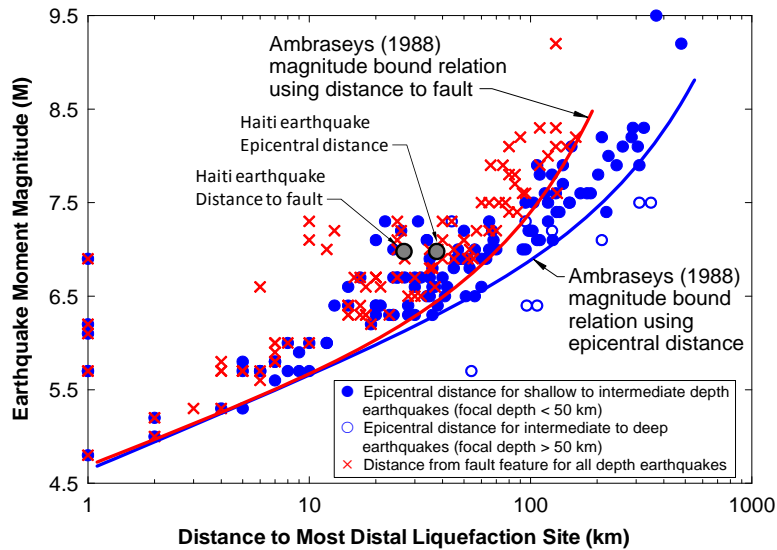


**Figure 7.2.** Comparison of most distal liquefaction sites identified in Haiti from aerial photography with worldwide data collected by Ambraseys (1988)

### **7.3 Coastal Failure west of L'acul**

Approximately 400 m of coastline at the mouth of a stream experienced significant translational movement west of the village of L'acul, as illustrated by the pre- and post-earthquake imagery in Figure 7.3. Also evident near the south end of the failure are uplifted coral beds, as described Section 4.0 Fault Rupture and Coastal Uplift. The primary manifestations of failure included cracking subparallel to the coastline (Figure 7.4 and Figure 7.5), a slump block near the northern extent of the failed zone, and sand blows near the southern extent of the failed zone (Figure 7.6). It is important to note that lateral spreads typically occurred in delta fan lobes or beach deposits adjacent to major stream discharge/delta zones. Lateral spread failures were rare or absent at points where coral has developed and "buttressed" the shoreline.

During reconnaissance efforts, the team conducted two dynamic cone penetration tests (DCPT) and two spectral analysis of seismic waves (SASW) lines at the site, one set near the sand blows at the southern end of the failed zone and one set outside of the failed zone to the south (Figure 7.3). Figure 7.7 presents the results of the DCPTs. As illustrated in Figure 7.7, the stratigraphy changes dramatically between the failed and non-failed zones, with loose sands being encountered near-surface within the failed zone and clays and peats being encountered near-surface outside of the failed zone. The fine-grained stratigraphy is expected because of its significant distance from the active mouth of the stream to the north. The results from SASW testing are still being processed and will be included in future versions of this report.

Based on the subparallel cracking, the formation of sand blows, and the results of the in-situ tests, the team attributed this failure to liquefaction and lateral spreading. Liquefaction likely occurred within the loose to medium dense sands below the watertable between depths of about 0.75 m and 2.3 m (2.5 to 7.5 ft). Below 2.3 m in the failed zone, the DCPT encountered much denser sands. The extent of the failure to the south was limited by the presence of fine-grained soils and peat overlying the denser marine sands.



**Figure 7.3.** Pre- and post-earthquake images of coastline near village of L'Acuil. Note in the lower, post-earthquake image the significant cracking subparallel to the coast and the arcuate slump in the northern end of the failure. SASW and DCPT testing was performed near several large sand blows located near the south end of the failure zone, as well as farther south outside of the failed reach. Imagery courtesy of Google Earth. Approximate center of image at 18°26'51.17"N, 72°41'11.06"W.



**Figure 7.4.** Cracking and lateral spread along coastline near village of L'Acul. (18°26'48.81"N, 72°41'11.92"W looking west).



**Figure 7.5.** Ground cracking along coastline near village of L'Acul. (18°26'48.83"N, 72°41'11.39"W looking west).



**Figure 7.6.** Sand blow formation to the south of the main cracks along coast near village of L'Acuil. ( $18^{\circ}26'44.27''N$ ,  $72^{\circ}41'12.05''W$  looking south).

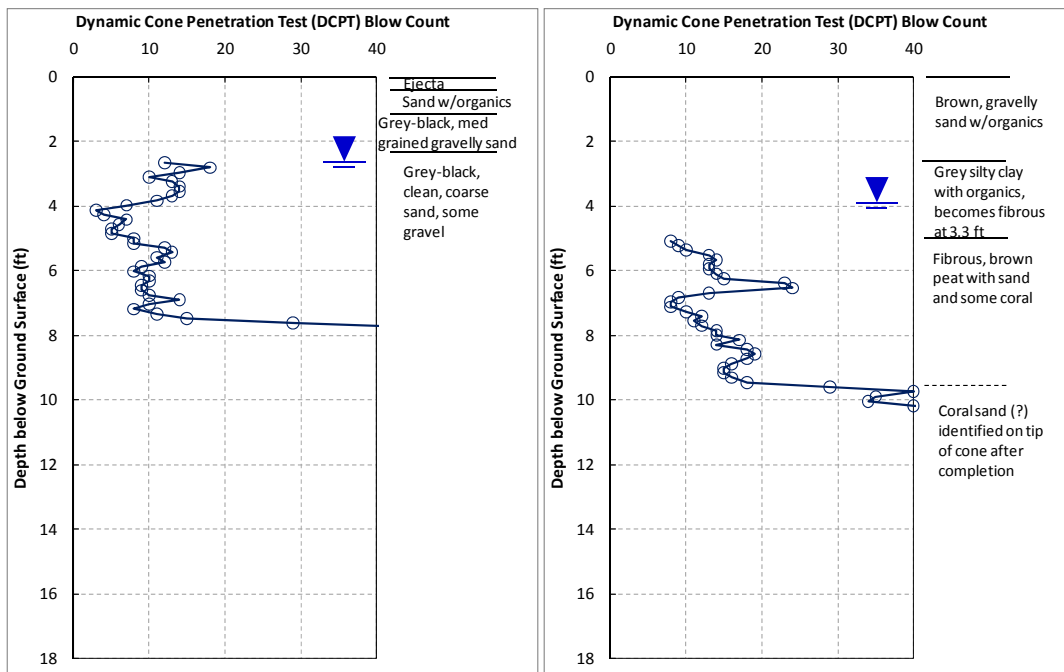


**Figure 7.7.** Results of DCPTs performed near coastline near village of L'Acuil. Sounding on left performed at south end of failed zone (DCPT-8), and sounding on right performed outside of failed zone (DCPT-9).

#### **7.4 Coastal Failure near Fouche**

Approximately 330 m of coastline failed near the village of Fouche, as illustrated in pre- and post-earthquake imagery in Figure 7.8. At this site, as much as 100 m of land (perpendicular to the coast) was lost as a result of the failure. The primary manifestations of failure included scarps, cracking, and graben formation in an arcuate path along the coastline (Figure 7.9 and Figure 7.10), as well as substantial damage to a stone wall running perpendicular to the coast and parallel to a braided stream that emptied into the bay (Figure 7.11 and Figure 7.12) and moderate-sized sand blows along the inland extent of the failure (Figure 7.13). One sand blow area included gravel clasts of up to about 2.5 cm in maximum dimension. The gravels may have been plucked from the sidewalls of the liquefaction feeder dike/fissure, or could have been entrained in the actual liquefied sediments.

During the reconnaissance efforts, the team conducted one DCPT and one SASW line near several sand blows at the eastern end of the failed zone (Figure 7.8 and Figure 7.14), and one SASW line outside of the failed zone to the east (Figure 7.8). A second DCPT was attempted in this non-failed area but a thick layer of fill precluded augering beyond a few inches. Figure 7.15 presents the results of the DCPT in the failed zone. As illustrated in Figure 7.15, loose sand was encountered at a depth of about 0.7 m (2.5 ft), underlying a low permeability cap layer consisting of clayey sand and silty clay. The sands became medium-dense to dense at a depth of about 1.6 m (5.5 ft). The results from SASW testing are still being processed and will be included in future versions of this report.

Based on the arcuate scarp, graben formation, sand blows development, and the results of the in-situ tests, the team attributed this failure to liquefaction and lateral spreading of the loose to medium dense sands below a depth of 0.7 m (2.5 ft). Headscarps and slump block scarps were up to 1.5 m high in the central parts of the failure, suggesting that failure extends perhaps 1.5 to 2 m below the original ground surface. Liquefaction likely extended to a depth of 1.6 m and may have occurred at greater depth, but penetration with the DCPT was limited in these denser sands. Similar to the coastal failure near the village of L'acul, this failure appears to coincide directly with the presence of the braided stream dumping loose sand into the sea, rather than in the marine sands present along the coast.



**Figure 7.8.** Pre- and post-earthquake images of coastline near village of Fouche. Note in the lower, post-earthquake image the significant loss of coast as outlined in blue. SASW-9 and DCPT-6 were performed near several moderate-sized sand blows located near the southeast end of the failure zone, while SASW-10 was performed outside of the failure zone. Imagery courtesy of Google Earth.



**Figure 7.9.** Scarp of coastal landslide near village of Fouche.  
( $18^{\circ}25'34.23''\text{N}$ ,  $72^{\circ}43'33.61''\text{W}$  looking northeastward)



**Figure 7.10.** Scarp of coastal landslide near village of Fouche.  
( $18^{\circ}25'34.01''\text{N}$ ,  $72^{\circ}43'34.60''\text{W}$  looking westward).



**Figure 7.11.** Damage to stone wall resulting from coastal failure and lateral spreading. (18°25'33.94"N, 72°43'34.27"W looking westward).

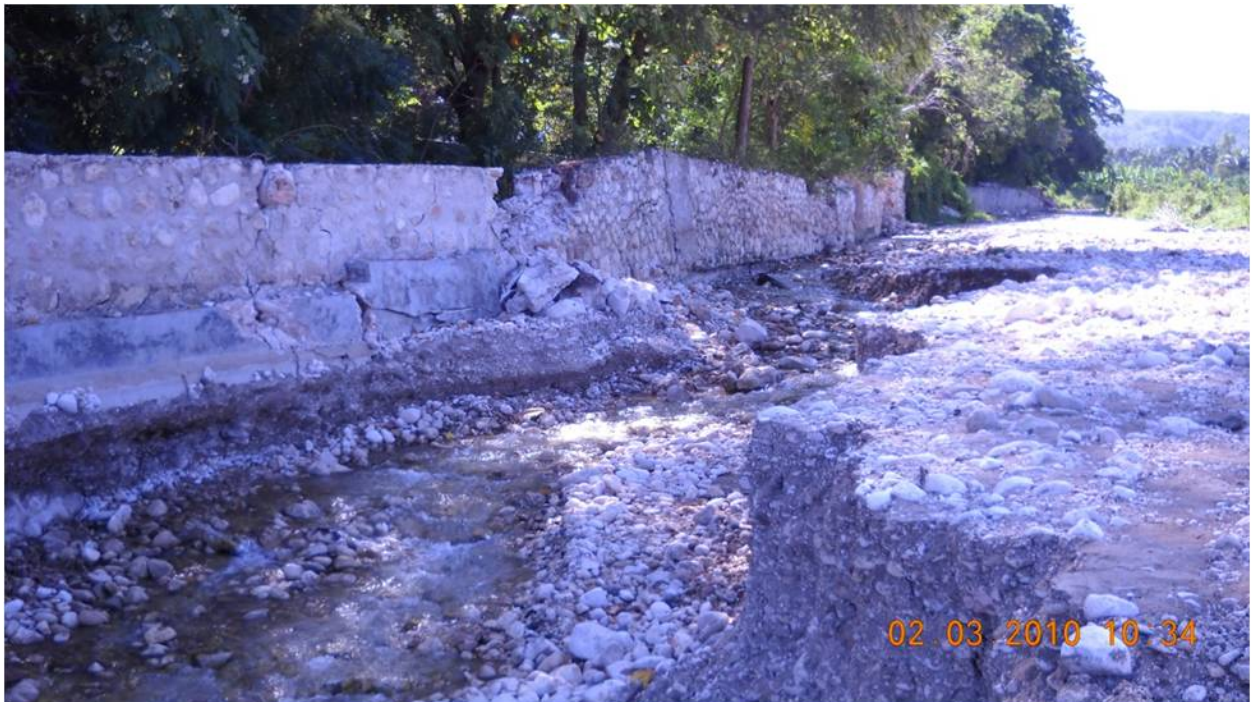


**Figure 7.12.** Damage to stone wall resulting from lateral spreading. Note the surficial cobbly material revealed by the failure scarp in the foreground. (18°25'33.31"N, 72°43'34.58"W looking southward away from coast).



**Figure 7.13.** Sand blow and ejecta formed at coastal failure site near village of Fouche. Approximate image coordinates: 18°25'35.08"N, 72°43'31.70"W.



**Figure 7.14.** DCPT and SASW testing performed at coastal failure site near village of Fouche. Approximate image coordinates: 18°25'35.12"N, 72°43'31.61"W.

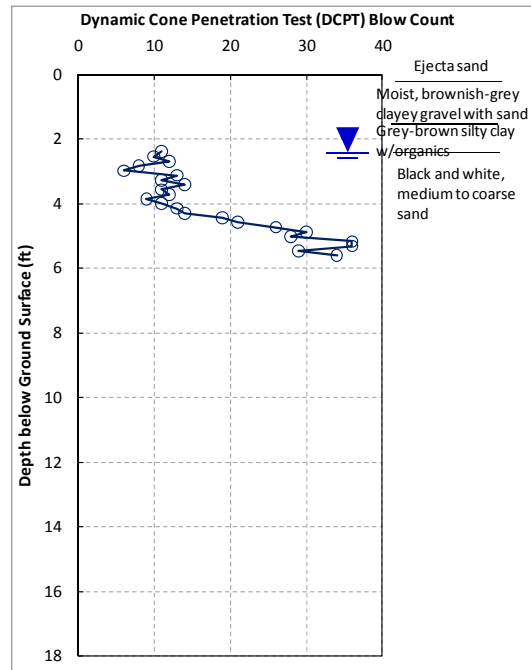


**Figure 7.15.** Results of DCPT-5 testing at coastal failure site near village of Fouche.

### 7.5 Coastal failure near Grand Goâve.

Approximately 400 m of coastline failed near the village of Grand Goâve, as illustrated in pre- and post-earthquake imagery in Figure 7.16. At this site, nearly 100 m of land (perpendicular to the coast) was lost as a result of the slide. The primary manifestations of failure included scarps (Figure 7.17 and Figure 7.18), cracking, and graben formation subparallel to the coastline (Figure 7.19), substantial damage to a unreinforced block wall running perpendicular to the coast (Figure 7.20), and small- to moderate-sized sand blows along the inland extent of the failure (Figure 7.21).

During reconnaissance, the team performed two DCPT and one SASW line near several sand blows at the inward end of the failed zone (Figure 7.16 and Figure 7.22). Figure 7.23 presents the results of the DCPT. As illustrated in Figure 7.23, loose sand to silty sand was encountered at a depth of about 0.8 to 0.9 m (2.6 to 3.0 ft), underlying a low permeability cap layer consisting of clayey silt. The sands became medium-dense to dense at a depth of about 1.1 to 1.6 m (3.6 to 5.3 ft). The results from SASW testing are still being processed and will be included in future versions of this report.

Based on the arcuate scarp, graben formation, sand blows development, and the results of the in-situ tests, the team attributed this failure to liquefaction and lateral spreading of the loose to medium dense sands and silty sands below a depth of 0.9 m. Liquefaction likely extended to a depth of 1.6 m and may have occurred at greater depth, but penetration with the DCPT was limited in these denser sands. Similar to the coastal failures near the villages of L'acul and Fouche, this failure occurred adjacent to a braided stream dumping loose sand into the bay (probably in a former channel of the stream), rather than in the marine sands present along the coast.

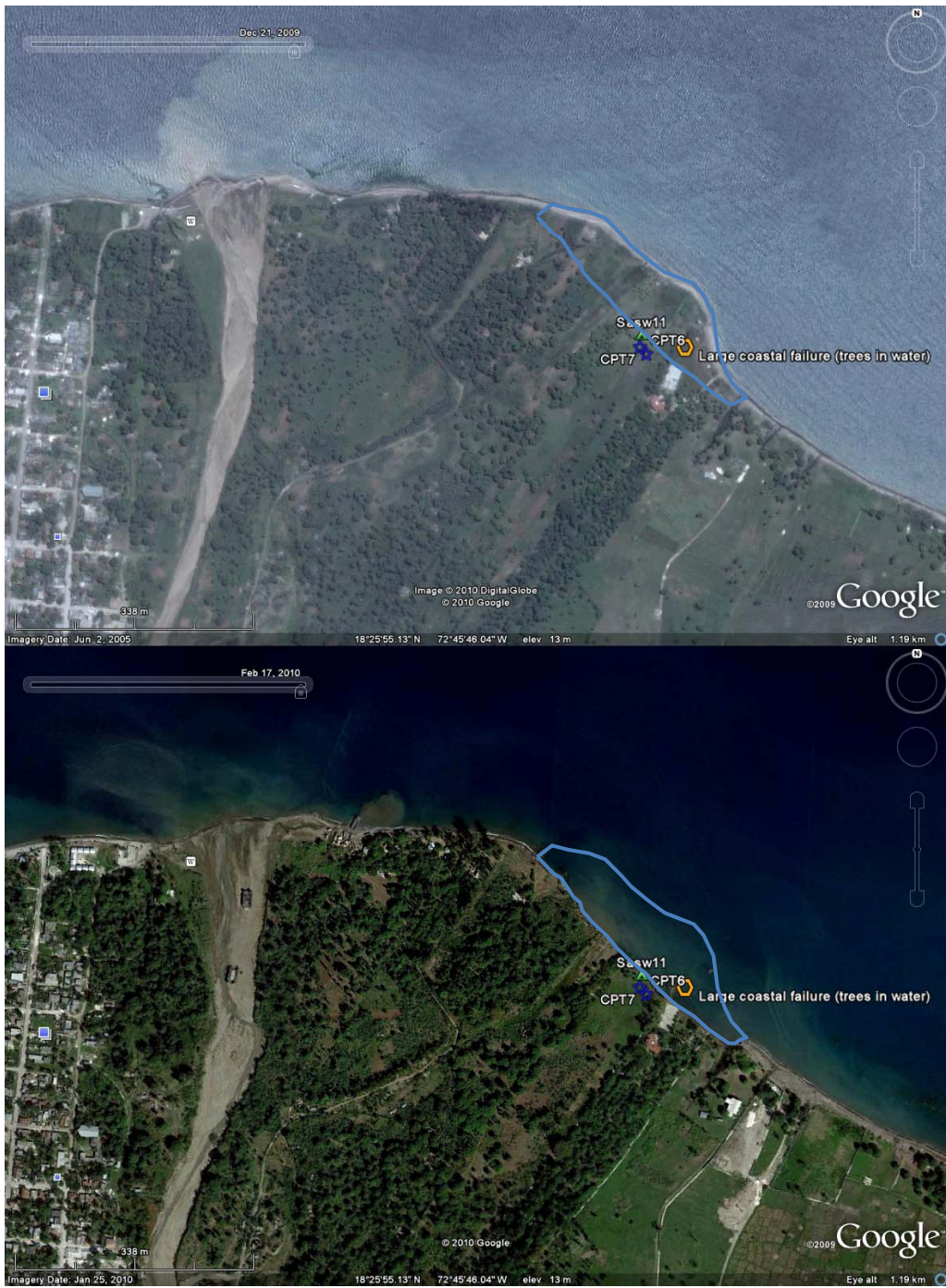


**Figure 7.16.** Pre- and post-earthquake images of coastline near village of Grand Goâve. Note in the lower, post-earthquake image the significant loss of coast as outlined in blue. SASW-11, DCPT-7, and DCPT-8 were performed just inland of the backscarp of the failed zone. Imagery courtesy of Google Earth.



**Figure 7.17.** Scarp formed along northern portion of coastal failure near village of Grand Goave. ( $18^{\circ}25'53.82''\text{N}$ ,  $72^{\circ}45'37.16''\text{W}$  looking northwest).



**Figure 7.18.** Scarp formed along southern portion of coastal failure near village of Grand Goave. ( $18^{\circ}25'52.91''\text{N}$ ,  $72^{\circ}45'35.92''\text{W}$  looking northwest)



**Figure 7.19.** Graben formation subparallel to coastline at coastal failure near village of Grand Goâve. ( $18^{\circ}25'54.43''\text{N}$ ,  $72^{\circ}45'37.99''\text{W}$  looking northwest).



**Figure 7.20.** Damage to unreinforced block wall running perpendicular to coast near village of Grand Goâve. ( $18^{\circ}25'51.84''\text{N}$ ,  $72^{\circ}45'38.06''\text{W}$  looking northeast).



**Figure 7.21.** Sand blow formation along inland extent of coastal failure near village of Grand Goâve. ( $18^{\circ}25'53.73''\text{N}$ ,  $72^{\circ}45'37.65''\text{W}$ )



**Figure 7.22.** DCPT and SASW testing at coastal failure site near village of Grand Goâve. ( $18^{\circ}25'53.64''\text{N}$ ,  $72^{\circ}45'37.76''\text{W}$  for left image,  $18^{\circ}25'54.16''\text{N}$ ,  $72^{\circ}45'37.85''\text{W}$  for right image)

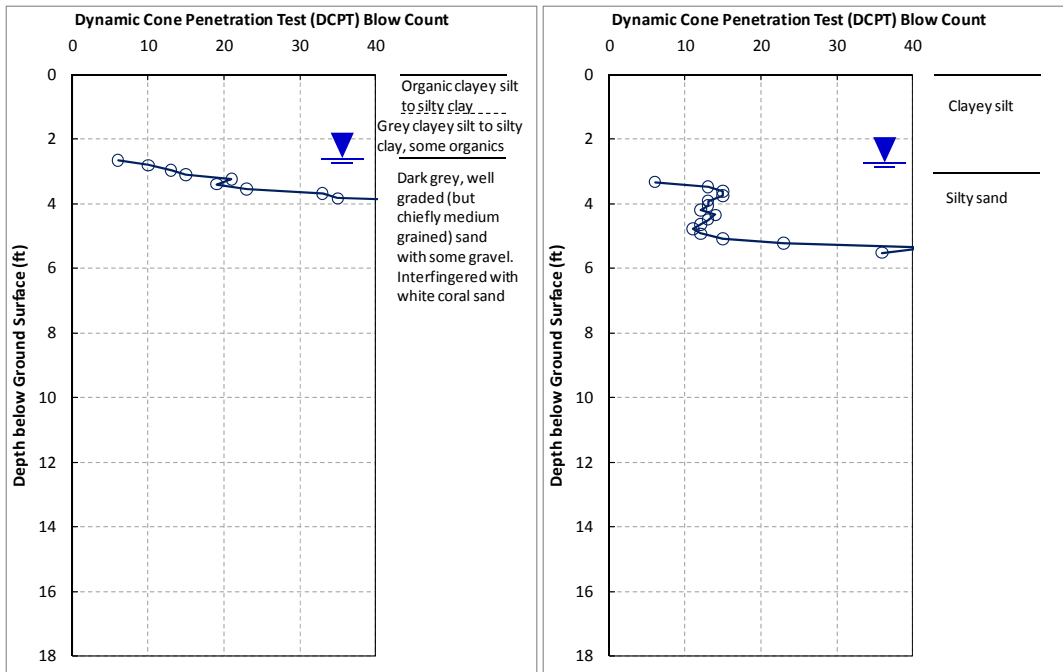


**Figure 7.23.** Results of DCPT-6 (at left) and DCPT-7 (at right) performed at coastal failure near village of Grand Goâve.

### References

Ambraseys, N.N. (1988). Engineering seismology. Earthquake Engineering and Structural Dynamics, 17, 1-105.

Olson, S.M., Green, R.A., Obermeier, S.F. (2005). Revised magnitude-bound relation for the Wabash Valley seismic zone of the central United States. Seismological Research Letters, 76(6), 756-771.

## 8.0 ROAD FILL PERFORMANCE

The GEER field reconnaissance included documentation and evaluation of several areas of road cracking/failure that occurred along the coastal Route 2 west of Carrefour, and a site of a road fill slump/settlement over a box culvert on Route 2 between Leogane and Dufort (Figure 8.1).

The investigated road fill failures represent the most notable or dramatic failures in the investigated reaches of the roadways, however many additional, typically smaller, road failures occurred in these areas, and presumably occurred in roadways that were not investigated by the GEER team. The investigated failures are believed, however, to provide a reasonable representation of the failure modes and road performance typical through the earthquake epicentral area.

The road failures documented included the following features:

- Large, continuous pavement cracks over about 1 to 5 cm in width, greater than 30-m in length, and causing adverse settlement or reduction of vehicle safety;
- Road crack/deformation features, or geometric characteristics suggestive of lateral spread or slumping of the road fill or of underlying natural foundation soils; and,
- Road failures that have been reported as possible examples of lateral spread or fault surface displacement.

In general, the investigated reaches of Route 2 follow relatively flat coastal benches or cross alluvial delta fan complexes near Carrefour and Leogane. Cut and fill grading has been used to raise road grade above small alluvial valleys and marshy areas, and to pass through small bedrock ridges. In cut/fill areas, fills typically are on the order of about 1 to 3 m thick with sideslopes ranging from about 1.5:1 to 2:1 (horizontal to vertical), occasionally with masonry or concrete walls at the toe of road fill slopes.



**Figure 8.1.** Index map of evaluated road fill failures by GEER team.



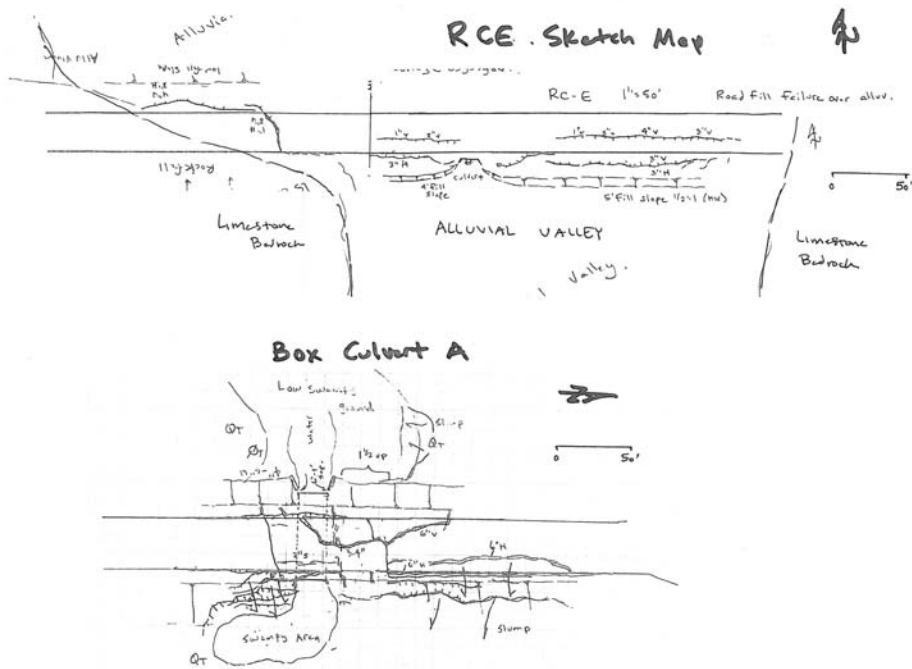


**Figure 8.3.** Road fill failure sketch maps for site RCE and BOXCLVTA.



**Figure 8.4** Typical arcuate road cracks at road failure site RCA west of Carrefour.

One notable site (BOXCLVT A) of road damage occurred between Leogane and Dufort, where a masonry box culvert passes under the roadway along a swampy area. The portion of the road bed over the culvert did not settle notably, but the prisms of fill against the culvert settled up to 30 cm. Discrete slumping of the road fills north and south of the culvert (Figure 8.5) damaged the outboard edges of the fill, contributing to the road failure. Fill exposed in large cracks (up to 30 cm wide) and slump headscarps consisted of well-compacted granular fill (Figure 8.6), and appeared to be suitably compacted. The settlement appears to have been caused by deformation in the soft, organic subgrade soils of the swampy zone, and slumping failure of the steep 1:1 to 1.5 :1 (horizontal to vertical) fill slopes that range from about 3 to 4.5 m high. This particular failure was previously reported to possibly represent surface fault rupture, as it occurs westward of the general trend of the Enriquillo-Plantain Garden fault trace. However, the reconnaissance team found no evidence of surface fault rupture west or east of the site, or along the fault trace in this area.

We did observe possible liquefaction features in a stream channel about 150 to 300 m south of the box culvert damage site. It is possible that liquefaction-induced soil failure or deformation contributed to the failure of the road subgrade, but liquefaction features were not observed at the box culvert site that instead were underlain by fine-grained organic soil.



**Figure 8.5** Cracks induced by fill slope slumping at road damage site BOXCLVTA.



**Figure 8.6** Well-compacted granular fill at road damage site BOXCLVTA.

## 9.0 LANDSLIDES

### 9.1 Introduction

Landslides were not pervasive in the near-fault region, but numerous failures did occur. Because of the large area affected by the earthquake, only a limited area of landsliding was investigated via field investigations. The field investigations predominantly consisted of observations during driving on major roads, and thus they only sampled a small fraction of the area affected by the earthquake. These field observations were supplemented by visual interpretation of aerial photographs using Google Earth.

### 9.2 Observations from Aerial Imagery

Figure 9.1 shows the landslides identified from aerial imagery by Dr. Ed Harp of the USGS. These landslides are concentrated in several regions: (1) along the deep, incised river valley that follows the fault trace, (2) along Route 204 about 15 km northwest of Jacmel, and (3) east of Route 204 about 10 km north of Jacmel. Smaller concentrations of landslides were observed near Provence in the west (Figures 9.2 and 9.3) and near Jacmel in the south. Failures observed in satellite imagery generally represent shallow slides (1 to 3 m thick) in which the overlying vegetation is stripped from the hillside. These types of failures have distinct features (i.e., bright, light colored areas surrounded by vegetation) that are easily identified in satellite imagery, but they must be large enough to be observed in the imagery.



**Figure 9.1** Landslides (red) identified by aerial imagery by Ed Harp of the USGS. Green track is route traveled by GEER team on day of landslide investigation. (Imagery from Google Earth)

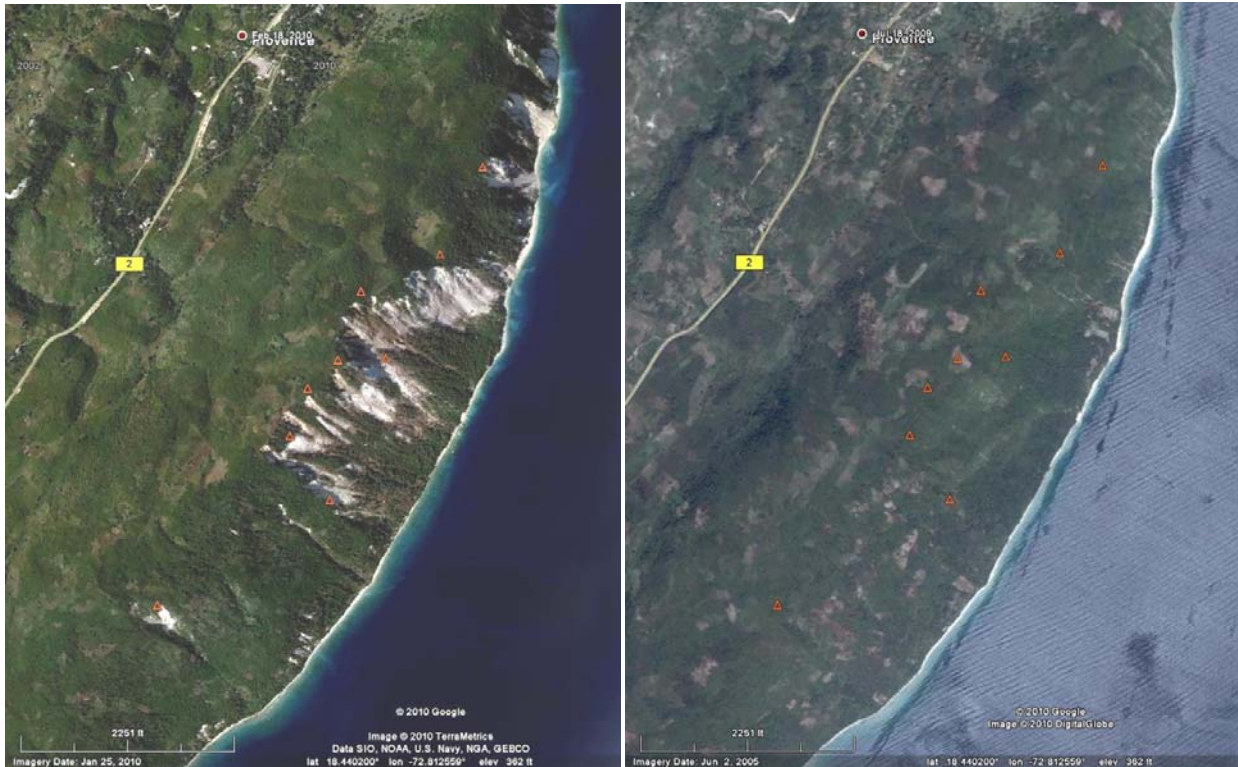


**Figure 9.2** Post-earthquakes denuded slopes due to landslides near Provence (left) along with pre-earthquake image (right). These are relatively steep ocean bluffs. (Scarp locations mapped by Ed Harp. Photos provided by Google Earth)



**Figure 9.3** Landslide scars near Provence in distance. (18.426166°N, 72.725825°E).

The concentration of landslides along Route 204 included many landslide dams that blocked two streams that flow east towards the road (Figure 9.4). These landslide dams were generated both by the debris of shallower soil slips, as well as deeper seated failures that appear to have been controlled by bedding. At least a few of these landslide dams breached in the weeks after the earthquake (Ed Harp, personal communication), but villages downstream were spared any inundation because the river valley was broad enough to accommodate the additional water.

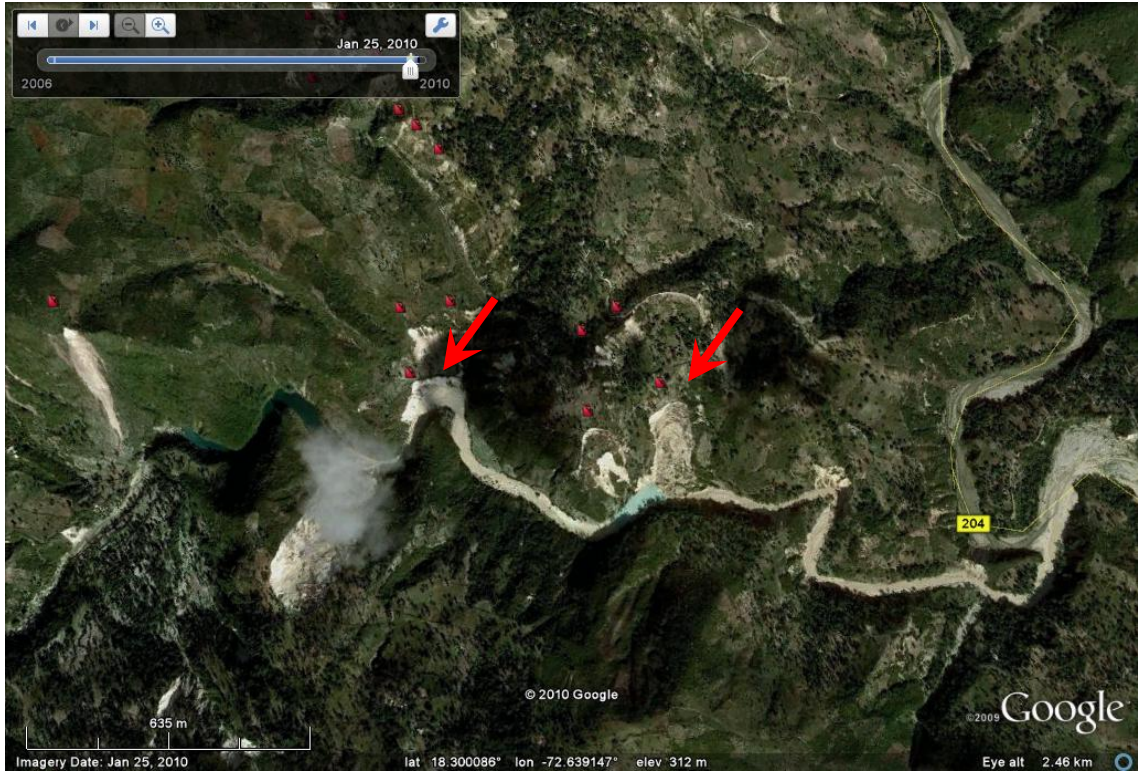
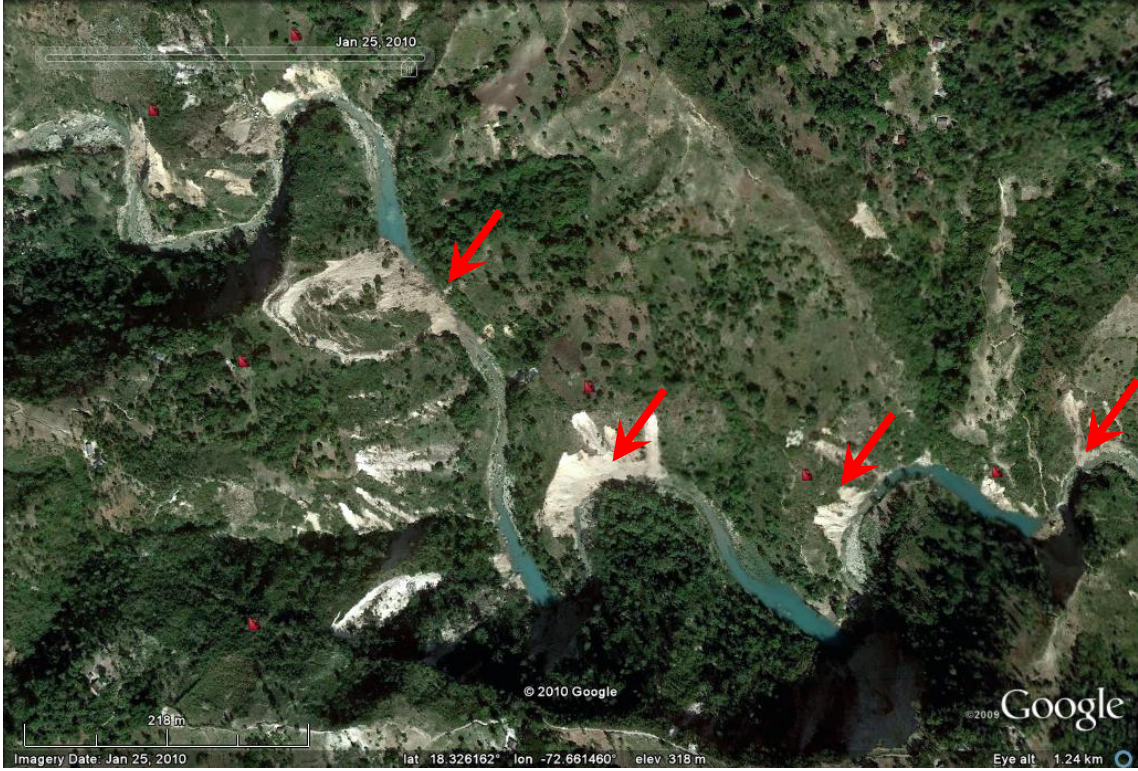


**Figure 9.4** Landslide dams (red arrows) and retained lakes west of Route 204 and approximately 15 km northwest of Jacmel (top: N18.326162, W72.66146, bottom: N18.300086, W72.639147).

### 9.3 Observations from Field Reconnaissance

In general, the slides observed during field reconnaissance occurred in over-steepened road cuts, over-steepened quarry walls, and over-steepened eroded stream banks. Most of the natural slopes that were observed performed well, as long as no over-steepening had occurred. Where over-steepening had occurred as a result of grading (e.g., road cuts), erosion, or quarrying, rockslides were common. The discussion of landslides in this section will focus on the hills of Petion-ville, south of Port-au-Prince, and on a 10 km segment of Route 204 south of Dufort. The segment of Route 204 investigated is shown in Figure 9.1.

Numerous topples or falls were observed in over-steepened road cuts in weathered and sheared bedrock within the hills of Pétiion-Ville (Figure 9.5), an upland suburb to the southeast of Port-au-Prince. These over-steepened cut slopes had estimated inclinations of  $\frac{1}{4}H:1V$  or steeper; many were nearly vertical and some remaining un-failed cuts were actually locally overhanging. These slopes had estimated heights on the order of 1.5 to over 6 m. The falls generally included relatively slender slivers, typically involving 0.3 to 1.0 m thick of material. The material fell to the base of the slopes, forming a wedge on the roadside or sidewalk, and frequently encroaching onto the roadway.

There were also many of these very steep road cuts that remained unfailed following the earthquake, as evidenced by the presence of vegetation, dust, and debris on the faces of the slopes (Figure 9.6). However, most of the unfailed slopes exhibited a wedge of raveled material at the base of the slope with established vegetation, suggesting the raveling had been occurring for some time and was not related to the recent earthquake, or with only minor toppling in the recent earthquake (e.g., Figure 9.5).

One area of more significant landslides was observed downhill from Petion-Ville along Rue Fernand. This landslide contained the rubble of several adjacent structures that had collapsed (Figure 9.7). There were scarp-like, near vertical surfaces near the top of slope, which could suggest that a rotational failure occurred beneath the now-collapsed structures. However, scarps of the observed height generated through a rotational failure would require a large volume of soil to be pushed out near the toe of slope. This volume of material did not appear to be present or to have been removed from the site. Furthermore, the soils are conglomeratic and likely have high friction angles, which would make the site an unlikely candidate for a rotational failure mechanism. It is more likely that the failure was initiated by basement/retaining walls for the overlying structures.



**Figure 9.5** Vertical cut remaining relatively stable with minor rock fall/topples.

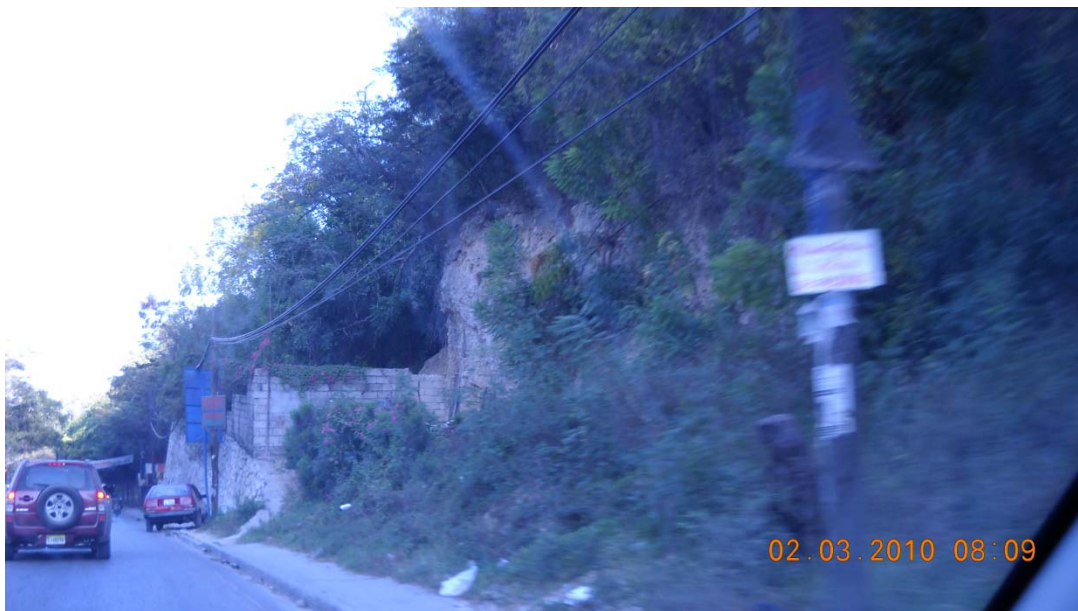


**Figure 9.6** Stable near-vertical road cut and masonry wall. (N18.531873, W72.313045).



**Figure 9.7** Several buildings have collapsed in this location. Although there are scarp-like near vertical surfaces near the top of slope that may suggest the possibility of a deeper rotation failure, in our opinion the observed conditions are likely due movement of soils adjacent to failed walls, as discussed in the text. (N18.528406, W72.309920).

There were numerous rock falls, rock topples, and shallow rockslides in over-steepened road cuts along Highway 204 (e.g., Figures 9.8 through 9.12), although few of these were obvious in the aerial imagery. Many of these failures, as well as similar failures elsewhere, inhibited relief supplies from reaching many upland communities. The cut inclinations where the majority of the failures occurred are estimated to be on the order of about  $\frac{1}{4}H:1V$  to  $\frac{3}{4}H:1V$ , and ranged from a few meters high to over 10 m high. The failures were frequently in fractured, friable, blocky sedimentary materials. These blocks were stacked in a statically stable configuration that did not resist the seismic accelerations, and the blocky material simply deaggregated and cascaded to the bottoms of the slopes. In some locations rockslides occurred along bedding planes, but more often the exposed scarp revealed that the bedding was relatively level or dipping into the slope and the failed material pulled away from random discontinuous surfaces.

Some chalky limestone quarries (recent activity of the quarries was not checked) had moderately high steep slopes that also failed in rock topples or rock falls. Occasionally these resulted in large boulders rolling onto roadways (Figure 9.8). Similar failures occurred in over-steepened road cuts through chalky limestone.



**Figure 9.8** Topple or fall included several large boulders in this old quarry.  
(N18.439010, W72.646168).

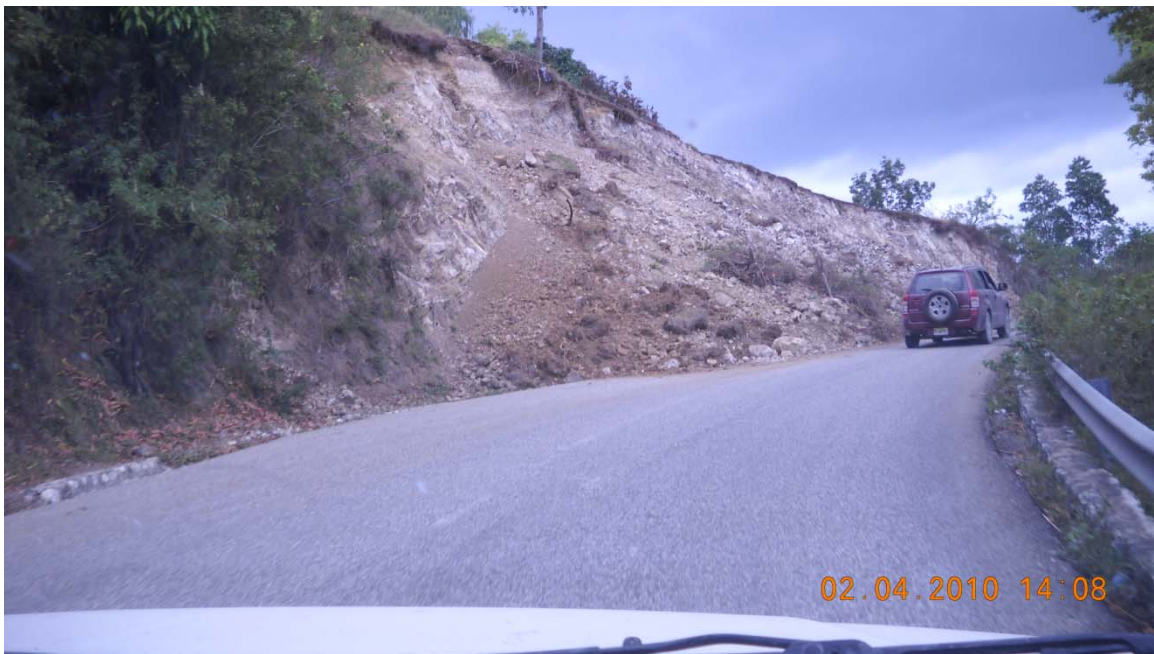


**Figure 9.9** Rock topple or rock fall from over-steepened road cut.  
(N18.412741, W72.638576).



**Figure 9.10** Shallow rock topple or rock fall from over-steepened road cut. Debris slid over the top of stable gabions at the toe of the slope. (N18.409159, W72.638815).



**Figure 9.11** Relatively shallow slip-out of regolith. Disaggregated material flowed over stable gabions and blocked over half the road. (N 18.409159, W72.638815).



**Figure 9.12** Shallow slip-out of soil in upper road cut. Soil slid over the top of the surviving masonry wall and slope protection. (N18.440270, W72.636207).